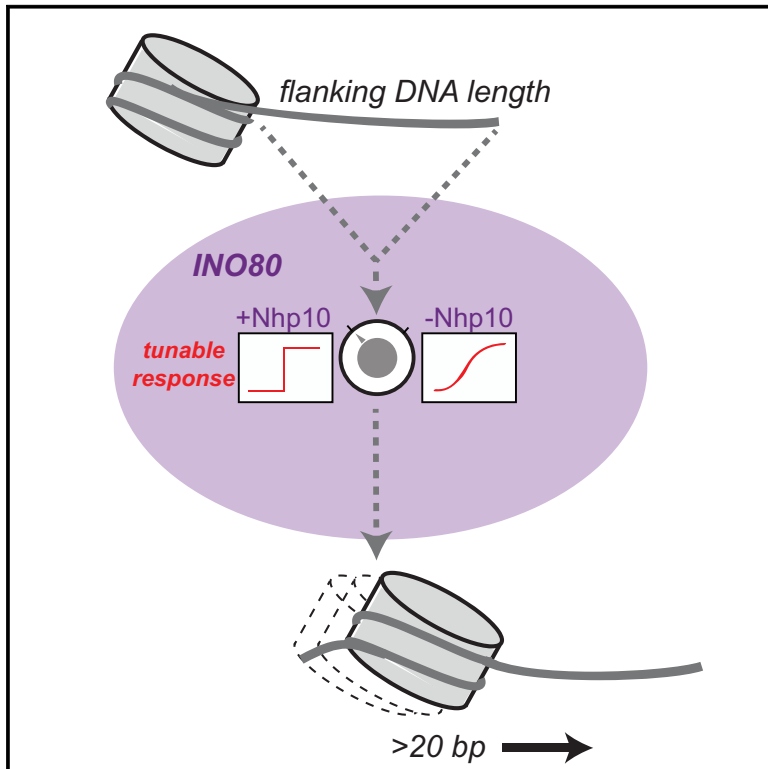


Molecular Cell

The Yeast INO80 Complex Operates as a Tunable DNA Length-Sensitive Switch to Regulate Nucleosome Sliding

Graphical Abstract



Authors

Coral Y. Zhou, Stephanie L. Johnson, Laura J. Lee, ..., Matthew J. Johnson, Ashby J. Morrison, Geeta J. Narlikar

Correspondence

geeta.narlikar@ucsf.edu

In Brief

The INO80 chromatin-remodeling complex has essential roles in DNA damage repair, DNA replication, and transcription, but it remains relatively poorly characterized. Here Zhou et al. use quantitative enzymology and single-molecule biophysics to describe a kinetic mechanism for nucleosome sliding by INO80, which likely has implications for INO80's specialized roles *in vivo*.

Highlights

- Nucleosome sliding by INO80 exhibits a switch-like response to flanking DNA length
- The Nhp10 module tunes the sliding response on nucleosomes with short flanking DNA
- INO80 rapidly slides a nucleosome >20 bp without re-assessing DNA length
- INO80 is highly processive and can move a nucleosome bi-directionally



The Yeast INO80 Complex Operates as a Tunable DNA Length-Sensitive Switch to Regulate Nucleosome Sliding

Coral Y. Zhou,^{1,2,5} Stephanie L. Johnson,^{1,5} Laura J. Lee,¹ Adam D. Longhurst,^{1,2} Sean L. Beckwith,³ Matthew J. Johnson,⁴ Ashby J. Morrison,³ and Geeta J. Narlikar^{1,6,*}

¹Department of Biochemistry and Biophysics, University of California, San Francisco, San Francisco, CA 94158, USA

²Tetrad Graduate Program, University of California, San Francisco, San Francisco, CA 94158, USA

³Department of Biology, Stanford University, Stanford, CA 94305, USA

⁴Google Brain, San Francisco, CA 94105, USA

⁵These authors contributed equally

⁶Lead Contact

*Correspondence: geeta.narlikar@ucsf.edu

<https://doi.org/10.1016/j.molcel.2018.01.028>

SUMMARY

The yeast INO80 chromatin remodeling complex plays essential roles in regulating DNA damage repair, replication, and promoter architecture. INO80's role in these processes is likely related to its ability to slide nucleosomes, but the underlying mechanism is poorly understood. Here we use ensemble and single-molecule enzymology to study INO80-catalyzed nucleosome sliding. We find that the rate of nucleosome sliding by INO80 increases ~100-fold when the flanking DNA length is increased from 40 to 60 bp. Furthermore, once sliding is initiated, INO80 moves the nucleosome rapidly at least 20 bp without pausing to re-assess flanking DNA length, and it can change the direction of nucleosome sliding without dissociation. Finally, we show that the Nhp10 module of INO80 plays an auto-inhibitory role, tuning INO80's switch-like response to flanking DNA. Our results indicate that INO80 is a highly processive remodeling motor that is tightly regulated by both substrate cues and non-catalytic subunits.

INTRODUCTION

Dynamic accessibility of a cell's genome is key to the regulation of DNA-based processes. In eukaryotes, these dynamics are ultimately gated by the nucleosome, the fundamental unit of chromatin, consisting of 147 bp of DNA wrapped around a core of eight histone proteins. ATP-dependent chromatin remodeling enzymes convert the chemical energy of ATP into mechanical forces that break and re-form histone-DNA contacts. These small-scale changes to nucleosome structure, coupled with the action of other chromatin factors, translate into large-scale changes to the chromatin landscape, and ultimately, they regu-

late every aspect of genome biology from transcription to DNA damage repair (Clapier and Cairns, 2009; Zhou et al., 2016). Of the four main families of remodelers (ISWI, SWI/SNF, CHD1, and INO80), the INO80 family is the most recently discovered and its biochemical mechanisms remain the most elusive (Morrison and Shen, 2009; Shen et al., 2000; Zhou et al., 2016).

The INO80 remodeler from *S. cerevisiae* is a multi-subunit complex consisting of a core remodeling ATPase (Ino80) and 14 other subunits (Morrison and Shen, 2009; Shen et al., 2000). *In vivo*, INO80 has roles in regulating transcription, DNA damage repair, replication, and metabolic regulation (Morrison and Shen, 2009; Yao et al., 2016). *In vitro*, INO80 slides mononucleosomes toward the center of short DNAs and spaces a tri-nucleosomal array (Udugama et al., 2011). Genome-wide studies have shown that ATP-dependent remodeling activity is required for establishing the specific nucleosome architecture at yeast promoters (Yao et al., 2016; Zhang et al., 2011). Using *in vitro*-reconstituted yeast chromatin, it was recently shown that INO80 is the only remodeler that is sufficient for positioning the +1 nucleosome at these promoters (Krietenstein et al., 2016), consistent with earlier data showing that several INO80 subunits bind specifically to the +1 nucleosome adjacent to the transcription start site (Yen et al., 2012, 2013). In combination with the known biochemical activities of INO80, these data suggest that the nucleosome-sliding activity of INO80 observed on single nucleosomes may play a critical role in positioning nucleosomes at the transcription start site, particularly the +1 nucleosome.

However, much is still unclear about the mechanism of nucleosome sliding by INO80, including how substrate cues are read by the enzyme and which motifs in the enzyme itself regulate this activity. Here we describe a combined approach using a variety of ensemble nucleosome-remodeling assays as well as single-molecule fluorescence resonance energy transfer (FRET) to probe the underlying mechanism of how yeast INO80 uses flanking DNA length as a substrate cue for nucleosome movement. We find that INO80 exhibits a switch-like response to flanking DNA length, consistent with and extending previous studies (Udugama et al., 2011). We further demonstrate that regulation of nucleosome sliding by flanking DNA length in INO80 is not



directly coupled to ATPase activity, unlike in the ISWI family (Whitehouse et al., 2003; Yang et al., 2006). Once sliding is initiated, INO80 rapidly slides a nucleosome at least 20 bp, and it is capable of sliding a nucleosome on a long stretch of DNA continuously and bi-directionally without dissociating. Finally, we describe an auto-inhibitory activity of INO80 that is specific for slowing sliding of nucleosomes with short flanking DNA. Taken together, our results suggest that INO80 has a distinct mechanism from other remodeling families, which likely has implications for INO80's specialized *in vivo* roles at the transcription start site and in double-strand break repair.

RESULTS

Flanking DNA Modulates the Overall Remodeling Rate of INO80, but Not Its ATPase Activity

Previous work using endpoint sliding assays has shown that yeast INO80 can slide mononucleosomes toward the center of a short DNA and evenly space a tri-nucleosomal array, but both activities require at least 50 bp of extranucleosomal DNA (Udugama et al., 2011). We used the strong nucleosome positioning sequence 601 to construct initially end-positioned nucleosomes with varying amounts of extranucleosomal DNA, and we found that, by native gel remodeling, efficient nucleosome sliding requires >40 bp of flanking DNA (Figure 1A), in agreement with this previous work (Udugama et al., 2011). We also noticed that, while nucleosomes with 60 bp of flanking DNA (0/60) are moved to a more centered position that runs as a single discrete band on a native gel, nucleosomes with 80 bp of flanking DNA (0/80) are slid toward the center, but they result in a final distribution of products that runs as a doublet on a native gel (Figure 1A). The appearance of this doublet is sequence specific (Figure S1A), suggesting that DNA sequence can affect the final product distribution. However, DNA sequence does not affect the rate of remodeling (Figures S1B–S1D), similar to what was reported for ISWI remodelers (Partensky and Narlikar, 2009) and for INO80 in a reconstituted yeast chromatin system (Krientein et al., 2016).

Thus, as shown previously, yeast INO80 exhibits a switch-like response to flanking DNA in terms of sliding outcome, requiring at least ~50 bp of flanking DNA for efficient sliding (Figure 1A; Udugama et al., 2011). To gain mechanistic insight into this behavior, we used a FRET-based assay to understand how the maximal rates of nucleosome sliding (k_{obs}) change as a function of flanking DNA length. We found that varying the flanking DNA from 40 to 80 bp increased the k_{obs} for remodeling by 300-fold (Figures 1B and 1C). However, the largest increase in rate constant (~100-fold) occurred when flanking DNA length increased from 40 to 60 bp. As these experiments were performed under saturating concentrations of INO80, the differences in rate constant arose from differences in a step that occurred post-binding.

Our observation that INO80's nucleosome-sliding activity is modulated by flanking DNA length is reminiscent of the well-studied ISWI remodeling enzymes, which move nucleosomes faster toward longer flanking DNA by coupling length sensing to the ATPase activity of the motor (Whitehouse et al., 2003; Yang et al., 2006). To test whether this paradigm holds true for

INO80, we measured the ATPase activity of INO80 when stimulated by nucleosomes with varying lengths of flanking DNA, using the same INO80 and nucleosome concentrations as in the FRET-based assay. Despite the 300-fold difference in the remodeling rate constant by FRET between 0/40 and 0/80 nucleosomes, INO80's ATPase activity stimulated by these two substrates was comparable (Figure 1D). This result is consistent with a previous study showing that increasing flanking DNA length results in a less than 2-fold effect on ATPase activity (Udugama et al., 2011), and it demonstrates that DNA length sensing by INO80 is not directly coupled to ATPase activity. Taken together, these findings stand in contrast to what has been shown for ISWI family motors, raising the possibility that the INO80 family uses a different mechanism to slide nucleosomes. These results also indicate that the substantially slower rate of sliding with 0/40 nucleosomes is not due to an inability of INO80 to bind these nucleosomes, because the rate of ATP hydrolysis with 0/40 nucleosomes is comparable to that with 0/80 nucleosomes.

Based on these observations, we hypothesized that the ATPase activity of INO80 is used to generate another type of remodeled intermediate that is not detected by native gel or FRET. To test this hypothesis, we used a restriction enzyme accessibility (REA) assay to measure rates of remodeling by INO80 (Figure 1E) (Narlikar et al., 2001; Polach and Widom, 1995). In principle, the REA assay can report on changes to the accessibility of the nucleosomal DNA arising from changes that do not require nucleosome sliding, such as DNA unpeeling. By REA, we found that nucleosomes with 40 bp of flanking DNA showed an increase in DNA accessibility at a maximal rate constant that was 10-fold faster than that observed by FRET ($0.05 \pm 0.02 \text{ min}^{-1}$ versus $0.005 \pm 0.006 \text{ min}^{-1}$, respectively) (Figures 1F and 1G). In the absence of ATP, changes in accessibility were substantially lower (Figure 1F). These observations suggest that INO80 can alter histone-DNA contacts of a nucleosome with shorter flanking DNA but cannot efficiently convert this altered nucleosome into a slid product, unless the nucleosome has >40 bp of flanking DNA. Interestingly, the 300-fold difference in k_{obs} between nucleosomes with 40 versus 80 bp of flanking DNA as measured by FRET decreased to 12-fold when measured by REA, suggesting that creation of the REA-sensitive intermediate versus a slid product depend differently on flanking DNA length. Importantly, this difference in k_{obs} as measured by REA did not appear to be the result of a difference in the stoichiometry of INO80 on the respective nucleosomes or artifactual differences between the REA and FRET-sliding assays (Figures S2D–S2H). Interestingly, we found that moving the restriction site to other positions along the nucleosomal DNA resulted in substantially decreased changes in accessibility (Figures S2A–S2C), suggesting that the DNA accessibility created by INO80 is restricted to the H2A/H2B surface. We note that we did not see evidence for dimer loss being essential for nucleosome sliding (Figures S1E–S1G).

Remodeling by INO80 Is Dominated by a Long Initial Pause, followed by Rapid Nucleosome Mobilization

Single-molecule FRET (smFRET) has proven to be a powerful tool for dissecting the individual kinetic steps in the remodeling

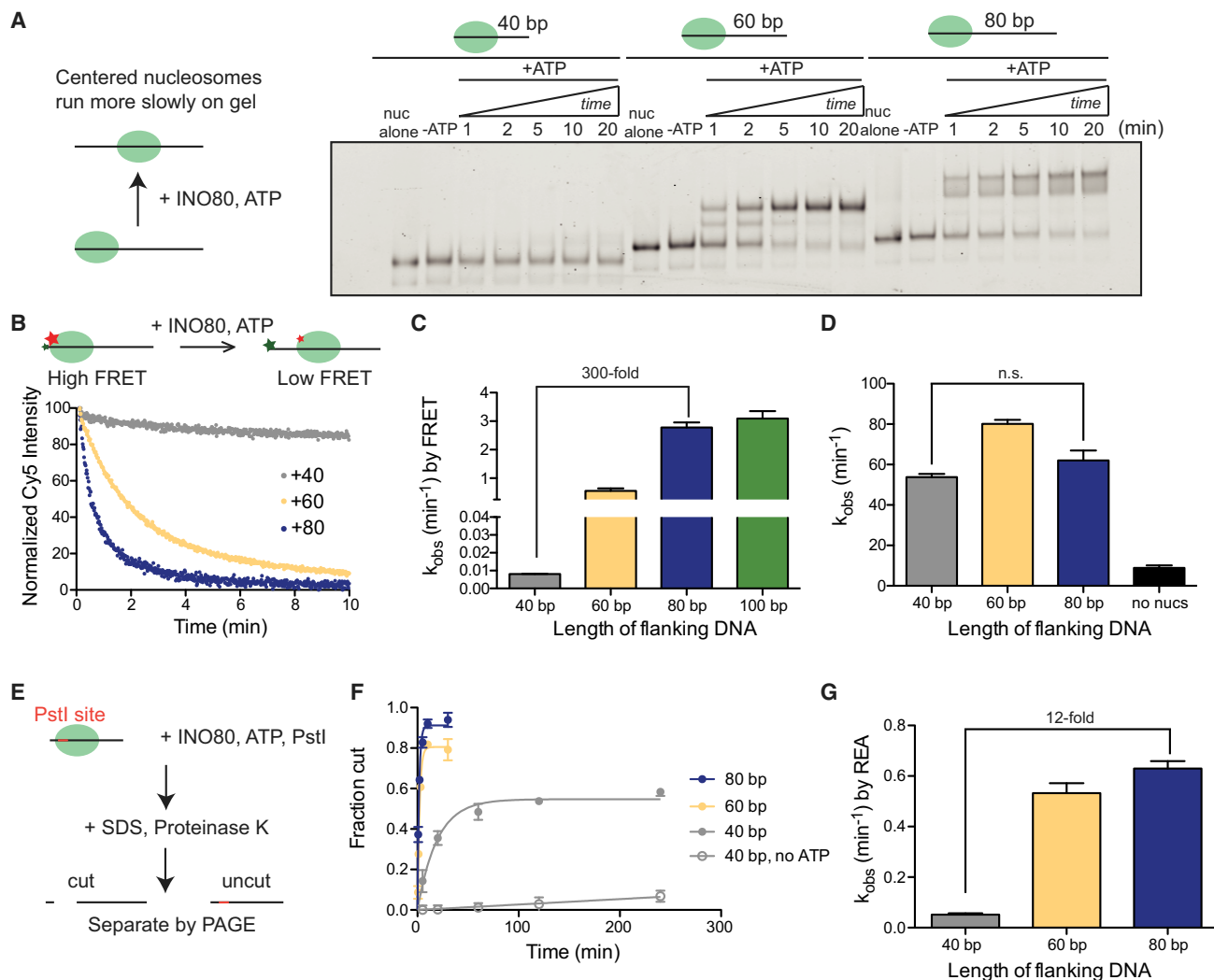


Figure 1. Flanking DNA Length Modulates Nucleosome Sliding by INO80, but Not ATPase Activity

(A) Left: schematic of the native gel assay. Right: native gel shows the remodeling of nucleosomes over time with 40, 60, or 80 bp of flanking DNA (0/40, 0/60, and 0/80 nucleosomes), under single-turnover conditions and with saturating enzyme and ATP.

(B) Left: schematic of the ensemble FRET-remodeling assay and example raw data for 0/40, 0/60, and 0/80 nucleosomes.

(C) Rate constants for remodeling of 0/40, 0/60, 0/80, and 0/100 nucleosomes by ensemble FRET. These assays were performed under single-turnover conditions and with saturating enzyme and ATP.

(D) Rate constants for ATP hydrolysis for 0/40, 0/60, and 0/80 nucleosomes derived from initial rates. These assays were performed under multiple turnover conditions, with INO80 in excess and saturating over nucleosomes and ATP in excess of INO80.

(E) Schematic of the REA assay. Remodeling by INO80 (DNA unpeeling, a conformational change, or nucleosome sliding) exposes a PstI site located 18 bp from the short end of the DNA. After digestion of the histones with Proteinase K, uncut and cut products are separated by native gel.

(F) Quantification of the fraction of the DNA cut by the PstI restriction enzyme as a function of time for 0/40, 0/60, and 0/80 nucleosomes.

(G) Quantification of the rate constant for cutting by PstI for 0/40, 0/60, and 0/80 nucleosomes. These assays were performed under single-turnover conditions and with saturating enzyme and ATP.

Data in (C), (D), and (G) represent the mean \pm SEM for three replicates.

reactions of other families, most notably the ISWI family (Blosser et al., 2009; Deindl et al., 2013; Harada et al., 2016; Hwang et al., 2014). We therefore adapted the smFRET assay to study INO80 to gain additional mechanistic insight. Figure 2B shows several examples of smFRET measurements of INO80 remodeling individual 3/78 nucleosomes. As expected, the overall FRET efficiency decreases over time, consistent with INO80 sliding the

nucleosome away from the DNA end. Although we cannot rule out the formal possibility that part or all of the observed change in FRET is due to a process other than sliding—for example, unpeeling of the DNA away from the octamer surface, which would also result in a change in inter-dye distance—we note that the behavior shown in Figure 2B is ATP dependent, with changes in FRET that are not instantaneous (Figure S3H).

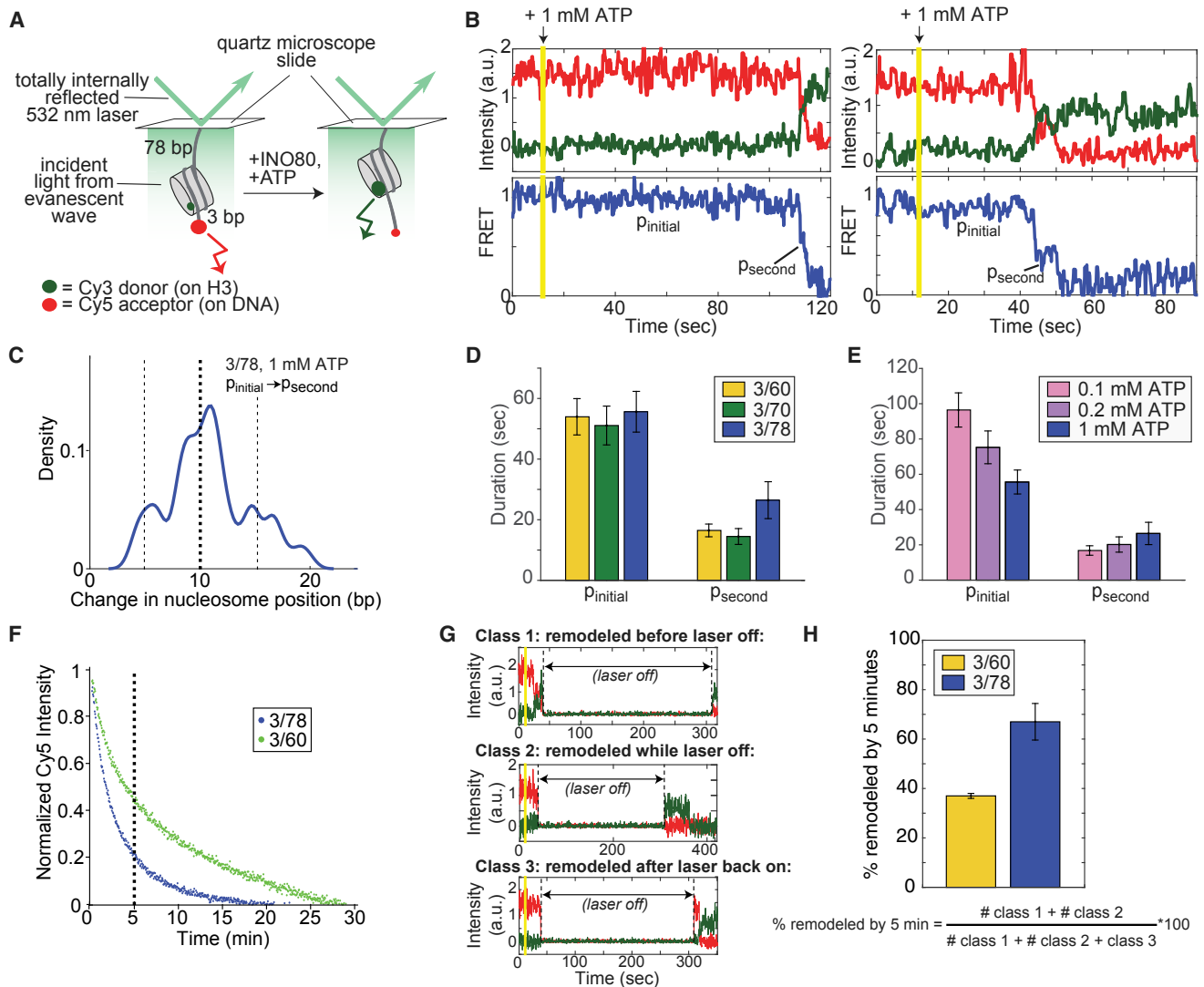


Figure 2. Remodeling by INO80 at the Single Nucleosome Level Is Preceded by a Long Pause, followed by Rapid Nucleosome Translocation (A) Schematic of the smFRET assay. Nucleosomes are immobilized on the surface of microscope slides and imaged with a prism-based total internal reflection fluorescence (TIRF) microscope (STAR Methods). For the 3/78 nucleosome shown here, the nucleosome starts 3 bp from the Cy5-labeled DNA end, with a 78-bp linker attaching the nucleosome to the surface, resulting in an initial high FRET efficiency (Figure S3A). As remodeling proceeds, the nucleosome is moved toward the 78-bp flanking DNA and the FRET efficiency is reduced.

(B) Example time courses of remodeling from individual, surface-attached, 3/78 nucleosomes in the presence of saturating INO80 and ATP (15 and 1 mM, respectively), imaged at 7.4 Hz and smoothed (for visualization only) with a median filter with a 1 s window. Vertical yellow line indicates the time at which ATP is introduced into the sample chamber to start the remodeling reaction. We refer to the long initial pause, exhibited by all trajectories, as P_{initial} , and to a secondary pause, exhibited in about three-quarters of remodeling events (Figures S3B and S3C), as P_{second} . Additional example time courses are shown in Figure S4.

(C) Kernel density estimation (KDE) plot of the change in nucleosome position between P_{initial} and P_{second} for the 78 3/78 nucleosomes (of 100 3/78 nucleosomes total with 1 mM ATP) that exhibit a secondary pause. KDEs are conceptually similar to histograms, but they have a smoothing parameter rather than a bin size (see also Figure S3). The peak in the density around 10 bp indicates that the majority of the trajectories that show secondary pauses on 3/78 nucleosomes have translocated the nucleosome about 8–12 bp before the secondary pause is encountered. KDE has a Gaussian kernel with bandwidth 0.025.

(D) Quantification of the average durations of the initial and secondary pauses, as a function of entry DNA length, for 3/60, 3/70, and 3/78 nucleosomes. Some traces exhibit more than one secondary pause; however, these traces are too few to accumulate sufficient statistics beyond the P_{second} pause.

(E) Quantification of the average durations of the initial and secondary pauses, as a function of ATP concentration, for 3/78 nucleosomes. 1 mM ATP is saturating while 0.1 and 0.2 mM are both sub-saturating, though still well above the K_m (Figures S3D and S3E; Udugama et al., 2011). Dark blue data are the same as in (C). The increase in P_{initial} duration with decreasing ATP concentration is greater than the error on the measurements; the slight decrease in P_{second} , however, is not. Data in (D) and (E) represent means \pm SEM obtained via a bootstrapping approach (STAR Methods).

(F) Overall remodeling rates for 3/60 and 3/78 nucleosomes, as measured by ensemble FRET, at 20°C in imaging buffer (STAR Methods), under single-turnover conditions and with saturating enzyme and ATP. Each curve is the average of two independent replicates as described in the STAR Methods. After 5 min (vertical

(legend continued on next page)

At a simple level, the example time courses in [Figure 2B](#) suggest INO80 shares some features previously described for ISWI remodelers. ISWI remodelers exhibit a stereotyped behavior when observed at the single-nucleosome level: remodeling proceeds through an alternating series of pauses, during which the FRET is constant and no change in nucleosome position is detected, and translocation events, during which the nucleosome is slid ([Blosser et al., 2009; Deindl et al., 2013; Hwang et al., 2014](#)). An emerging model is that the pauses in the ISWI reaction represent a rate-limiting regulatory step, during which substrate cues are periodically assessed and used to gate translocation activity ([Zhou et al., 2016](#)). Nucleosome sliding by INO80 similarly appears to contain pause and translocation phases: the reaction begins with an extremely long pause (about a minute long on average; [Figure 2D](#)), and translocation is often interrupted (about 75% of the time; [Figures S3D and S3E](#)) by at least one additional pause that appears to occur at roughly half-maximal FRET ([Figures 2C, S3D, and S3E](#)). These pauses are candidates for regulatory steps as in the ISWI paradigm and are discussed further below. Translocation itself is fast, even at 20°C (~7 bp/s at saturating ATP; [Figure S3H](#)), comparable to the translocation rate of the ISWI family member ACF at 30°C (~7–9 bp/s; [Blosser et al., 2009](#)). As discussed in the next section, however, these similarities between the INO80 and ISWI reactions do not extend beyond a qualitative level.

The Initial Pause Is ATP Dependent, but Not DNA Length Sensitive

Analogous to INO80, many ISWI remodelers are sensitive to flanking DNA length ([He et al., 2006; Whitehouse et al., 2003; Yang et al., 2006; Zofall et al., 2004](#)). smFRET studies with ISWI remodelers have shown that DNA length sensing occurs during the pause phases of remodeling: increasing flanking DNA length decreases the durations of the pauses, but it does not affect translocation rates ([Blosser et al., 2009; Hwang et al., 2014](#)). Furthermore, a reduction in ATP concentration results in longer pauses and slower translocation for ISWI complexes, implying that ATP is required for both the pause and translocation phases ([Blosser et al., 2009; Deindl et al., 2013; Hwang et al., 2014](#)).

We performed similar experiments with INO80 to ask which step(s) in its remodeling reaction are sensitive to flanking DNA length or ATP concentration. For these experiments, we used nucleosomes containing flanking DNA lengths of 60, 70, or 78 bp, and we varied ATP concentration from 0.1 to 1 mM. As with ISWI remodelers, the translocation phases of INO80 were sensitive to ATP concentration and not to flanking DNA length ([Figure S3H](#)). The initial pause (p_{initial} in [Figure 2B](#)) was sensitive

to ATP concentration, but surprisingly, it was not sensitive to flanking DNA length ([Figures 2D and 2E](#)). The ATP dependence of p_{initial} quantitatively recapitulated the ATP dependence of the overall remodeling rate constant measured by ensemble FRET, suggesting that p_{initial} contains the main ATP-dependent step observed in ensemble assays ([Figure S3G](#)).

Even more surprisingly, the secondary pauses were not sensitive to either flanking DNA length or ATP concentration ([Figures 2D and 2E](#)). If either p_{initial} or p_{second} was sensitive to flanking DNA length, we would have expected these pause durations to decrease with increasing flanking DNA. However, we did not observe a statistically significant trend in either p_{initial} or p_{second} as a function of increasing flanking DNA length from 60 to 80 bp ([Figure 1C](#)). These results suggest that the secondary pauses do not play a regulatory role in nucleosome sliding. Rather, we favor an interpretation of our results in which the secondary pauses of the INO80 remodeling reaction are a consequence of how the nucleosomal DNA wraps around the histone octamer. The regulatory pauses in ISWI are non-random, with the first pause occurring before an initial large (~7 bp) translocation event and the subsequent pauses occurring before smaller (~3 bp) translocation events, independent of DNA sequence ([Blosser et al., 2009; Deindl et al., 2013; Hwang et al., 2014](#)). In contrast, the secondary pauses in the INO80 reaction occurred predominantly after 10 bp of movement and less commonly after 5 or 15 bp of movement ([Figures 2C, S8B, and S8C](#)). These values are intriguingly close to the rotational periodicity of nucleosomal DNA ([Luger et al., 1997](#)). Furthermore, the distribution of the locations at which p_{second} occurred, but not the pause durations, was sensitive to DNA sequence ([Figures S4F and S4G](#)), consistent with INO80 pausing at sites where the DNA forms favorable contacts with the histone core ([Hall et al., 2009](#)).

These results have important implications for the mechanism of remodeling by INO80: it appears that, once translocation has begun, it is not interrupted by regular pauses that allow re-interrogation of flanking DNA length after the nucleosome has been moved a short distance, at least not within the 20–25 bp for which the nucleosome is in FRET range ([Figure S3B](#)). For comparison, the ISWI family remodeler ACF, which has a similar length-sensing regime to INO80 in terms of the modulation of its overall remodeling rate, has about three length-sensitive pauses within the first 20 bp of nucleosome movement ([Blosser et al., 2009](#)).

Comparing our smFRET and ensemble FRET data raises a paradox, as flanking DNA length modulates the overall rate of INO80 remodeling as measured by ensemble FRET ([Figure 1C](#)), but it does not appear to modulate any step as observed by

dashed line), the ensemble-remodeling reaction on 3/78 nucleosomes is nearly 80% complete, while the reaction on 3/60 nucleosomes is only about 50% complete.

(G) Example time courses of remodeling of 3/60 nucleosomes in the presence of 1 mM ATP, with the laser that excites the Cy3 dye turned off for 5 min as indicated. While the laser is off, all dye intensities go to zero. Three kinds of behavior are observed: some nucleosomes are remodeled before the laser is turned off (class 1, top); some nucleosomes are remodeled after the laser is back on (class 3, bottom); and some nucleosomes have high Cy3 intensity before the laser is turned off, but high Cy3 intensity when the laser is turned back on (class 2, middle). These class 2 nucleosomes must have remodeled during the 5 min that the laser was off, because no change in Cy3 signal is observed with the laser off in the absence of ATP.

(H) Quantification of how many nucleosomes are remodeled in the first 5 min of the smFRET reaction when the laser is turned off as in the examples in (G). Data represent means \pm SEM for three replicates, where the fraction remodeled was calculated for each replicate according to the expression below the bar graph.

smFRET (Figures 2D and S3). In reconciling these differences, we noticed that the overall remodeling rate by ensemble FRET was slower than the remodeling we observed at the single-nucleosome level (Figure S4E), which was a significant departure from previous smFRET results with, for example, ISWI family remodelers, for which ensemble and smFRET remodeling rates correspond well (Blosser et al., 2009). We therefore hypothesized that photobleaching, which affects smFRET, but not ensemble FRET, measurements, may be masking a slow phase of the overall remodeling reaction and that this slow phase might be DNA length sensitive.

To test this possibility, we reduced the photobleaching effect by acquiring smFRET movies during which the imaging laser was turned off for 5 min early in the reaction (Figure 2G). Photobleaching of the fluorescent dyes occurs only when the laser is on. If the photobleaching process were the cause of the discrepancy we observed between ensemble FRET and smFRET, then the fraction of 3/60 versus 3/78 nucleosomes remodeled during these 5 min in the dark should mirror the fraction of the corresponding ensemble FRET reactions that had gone to completion in 5 min. Under smFRET buffer conditions, the ensemble FRET reaction went to ~50% and ~80% completion by 5 min for 3/60 and 3/78 nucleosomes, respectively, consistent with a flanking DNA length dependence (Figure 2F). Similarly, by smFRET we found that ~40% and ~70% of 3/60 and 3/78 nucleosomes, respectively, were remodeled after 5 min (Figure 2H). Thus, without photobleaching, we now observed a flanking DNA length dependence at the single-nucleosome level that mirrored what we observed by ensemble FRET. We therefore conclude that the INO80-remodeling reaction consists of a fast, DNA length-*insensitive* population that we observe under continuous laser illumination, and a slower, DNA length-sensitive population that we observe only when the masking effect of photobleaching is removed (see the Discussion).

INO80 Processively and Continuously Moves a Centered Nucleosome Significant Distances Back and Forth along the DNA

The results of Figure 2 suggest a potentially important feature of INO80's mechanism: processivity, which we define as a measure of how many base pairs the nucleosome can be translocated before dissociation of INO80. The experiments in Figure 2 were performed under chase conditions, and INO80 was observed under these conditions to slide end-positioned nucleosomes at least 20 bp, as discussed above. To more directly test for processivity, we generated FRET-labeled 78/78 nucleosomes, with the 601 positioning sequence flanked on both sides by 78 bp. We also moved the Cy5 dye to an internal position 9 bp from the nucleosome edge, which increased the distance for which the nucleosome was in FRET range on both sides of the nucleosome's initial starting point, so that back-and-forth motion of the nucleosome could be measured (Figures 3A and S3A).

Consistent with recent work with human INO80 (Willhoft et al., 2017), we found by gel remodeling that yeast INO80 mobilized this 78/78 construct, yielding a distribution of nucleosome positions, some of which were off-center (Figure 3B). Similarly, we found by smFRET that INO80 quickly slid these nucleosomes out of FRET range, as with the end-positioned constructs (Fig-

ure 3C). INO80 was also capable of sliding a nucleosome back and forth along the DNA without releasing it, as indicated by the alternating gains and losses of FRET in the observed bi-directional and multi-directional remodeling behaviors (Figure 3C). These results indicate that INO80 can catalyze many rounds of translocation without dissociating.

To confirm that the bi-directional, processive behavior we observed was due to the same INO80 complex that initially bound the nucleosome, we performed double-chase experiments, in which a second buffer exchange into 1 mM ATP was performed roughly a minute after the addition of ATP that started the remodeling reaction (Figure 3C, bottom panels). As a control, we also chased with buffer only, which stopped remodeling, indicating that we were fully exchanging the buffer in the sample chamber during these washes (Figure 3D). Thus, INO80 is capable of moving a nucleosome long distances bi-directionally along a DNA strand without dissociating. Although it is currently not clear how INO80 switches its direction of translocation under chase conditions, one possibility is that it can bind a nucleosome as a dimer. Cooperative binding and sliding of nucleosomes by two INO80's has recently been suggested for a human INO80 core complex (Willhoft et al., 2017).

Deletion of *nhp10* Results in Impaired Length Sensing by INO80

We next investigated what motif(s) in INO80 might be involved in regulating the switch-like increase in nucleosome sliding upon increasing flanking DNA length beyond 40 bp. Studies of both yeast INO80 (Tosi et al., 2013) and human INO80 (Chen et al., 2013) have shown that the complex is organized into modules, each composed of 3–4 subunits that make distinct contributions to nucleosome remodeling. For example, the Arp8 module, composed of Arp8, Arp4, Act1, Taf14, and Ies4, is marginally involved in nucleosome and DNA binding, but it is critical for the catalysis of nucleosome remodeling (Chen et al., 2013; Tosi et al., 2013). In contrast, the yeast-specific Nhp10 module, composed of Nhp10, Ies1, Ies3, and Ies5, is not critical for nucleosome movement or ATP hydrolysis, but it exhibits strong DNA- and nucleosome-binding properties on its own (Shen et al., 2003b; Tosi et al., 2013). Based on this observation, we hypothesized that the Nhp10 module may contribute to INO80's ability to discriminate between nucleosome substrates based on flanking DNA length.

To test this possibility, we purified INO80 complexes from yeast containing a deletion of *nhp10*. As seen previously, when compared to wild-type (WT) INO80 on an SDS-PAGE gel, the INO80(Δ *nhp10*) complex shows the absence of bands corresponding to components of the Nhp10 module, such as Ies3 (purple star, Figure 4A) (Shen et al., 2003a; Tosi et al., 2013). We also noticed that, in our purifications of INO80(Δ *nhp10*), the majority of the Ino80 band migrated faster on an SDS-PAGE gel than in WT INO80 (green star, Figure 4A), which we reasoned may correspond to a truncation of Ino80 that occurred as a result of deleting *nhp10*. Based on mass spectrometry data, we indeed found that the first ~200 amino acids of the N terminus of Ino80 were missing in INO80(Δ *nhp10*) but remained intact in WT INO80 (Figure S5A). Previous work has shown that the Nhp10 module interacts with these first 200 amino acids of

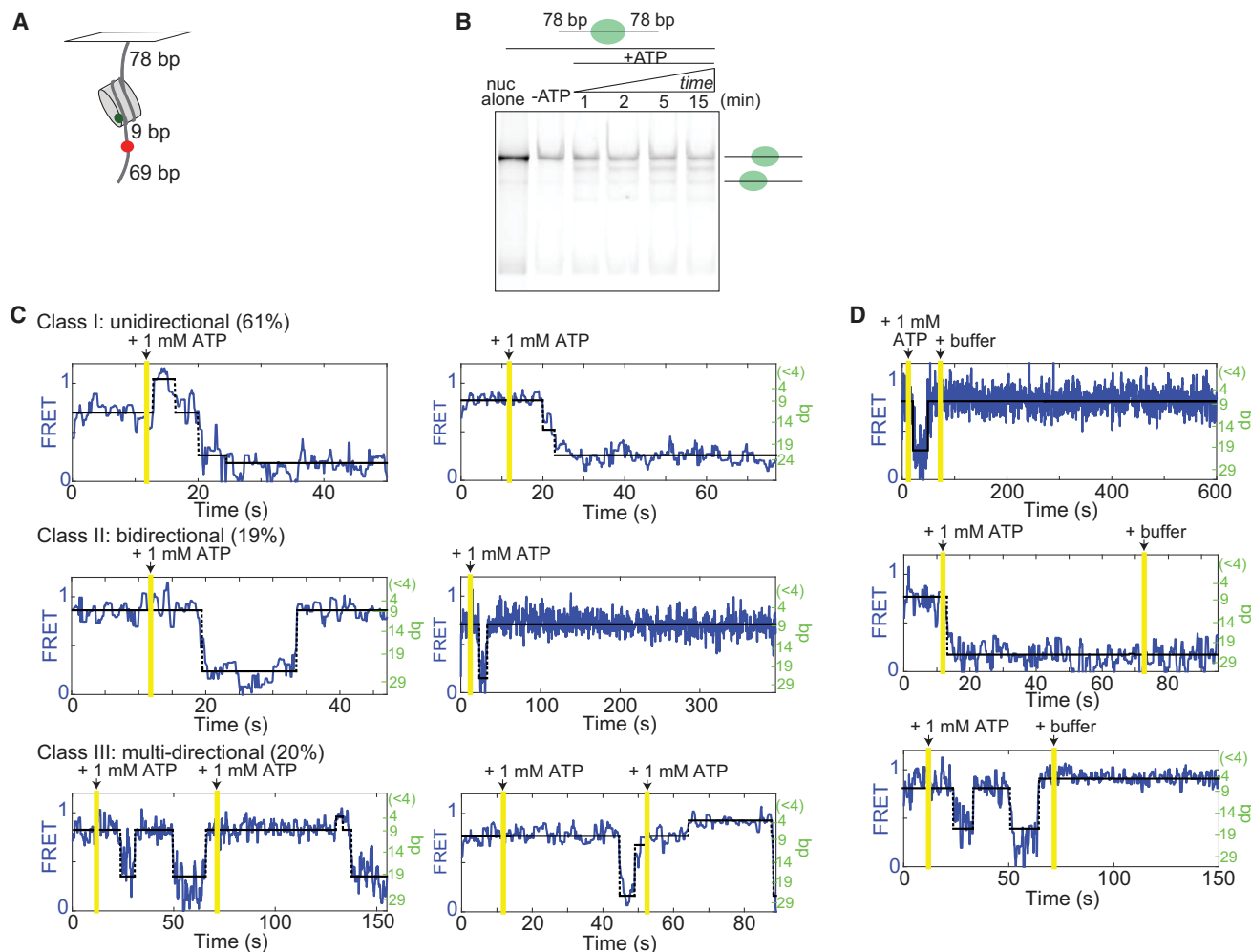


Figure 3. INO80 Processively and Continuously Moves a Nucleosome Bi-directionally on Long DNA

(A) Schematic of the centered 78/78 construct. These nucleosomes have an internal Cy5 9 bp from one edge of the 601 sequence that initially positions the nucleosome, such that they start in mid-high FRET (Figure S3A). If INO80 slides the nucleosome toward the surface, the FRET will decrease according to our calibration curve (Figure S3B); if the nucleosome is moved toward the dye, the FRET will increase and then decrease as the dye-labeled DNA base pair enters the nucleosome.

(B) Native gel showing the remodeling of the 78/78 nucleosomes in (A), under single-turnover conditions and with saturating enzyme and ATP. Remodeling was performed at 20°C for consistency with smFRET experiments.

(C) Example traces of remodeling of 78/78 nucleosomes with saturating INO80 and ATP (15 nM and 1 mM, respectively). See the STAR Methods for a description of the three classes of behavior. The two class III examples illustrate double-chase experiments. The percentages of the ~100 total traces (from the single-chase and double-chase experiments combined) that we classified into each type of behavior are given in parentheses. One of the class I traces has not been assigned a base pair scale on the right axis because it represents movement of the Cy5 into the nucleosome, where our calibration curve is not valid. The percentage of trajectories showing direction reversals with these initially centered constructs is double the percentage with end-positioned constructs (40% for the 78/78 construct versus 20% of all end-positioned constructs in Figure 2).

(D) No remodeling was observed after a second chase into buffer only (no ATP).

Ino80 (Tosi et al., 2013), suggesting that deletion of *nhp10* causes both the loss of the Nhp10 module from the INO80 complex as well as the destabilization and degradation of the N-terminal region of the Ino80 ATPase. To further test this possibility, we purified INO80 complexes from yeast containing an N-terminal deletion of Ino80. The INO80(Δ 2-200-*ino80*) complexes lacked the same subunits of the Nhp10 module (Figure 4A), further supporting the idea that the N terminus of Ino80 and the Nhp10 module are structurally inter-dependent.

We next compared the remodeling rates of these different mutant INO80 complexes on nucleosomes with 40-, 60-, or 80-bp flanking DNA, using ensemble FRET. We found that neither INO80(Δ 2-200-*ino80*) nor INO80(Δ *nhp10*) had a defect in remodeling nucleosomes with 80-bp flanking DNA, consistent with published data (Tosi et al., 2013). However, to our surprise, we observed a 100-fold increase in remodeling activity on nucleosomes with 40 bp of flanking DNA with the mutant complexes compared to WT INO80 (Figure 4B). In contrast, remodeling of

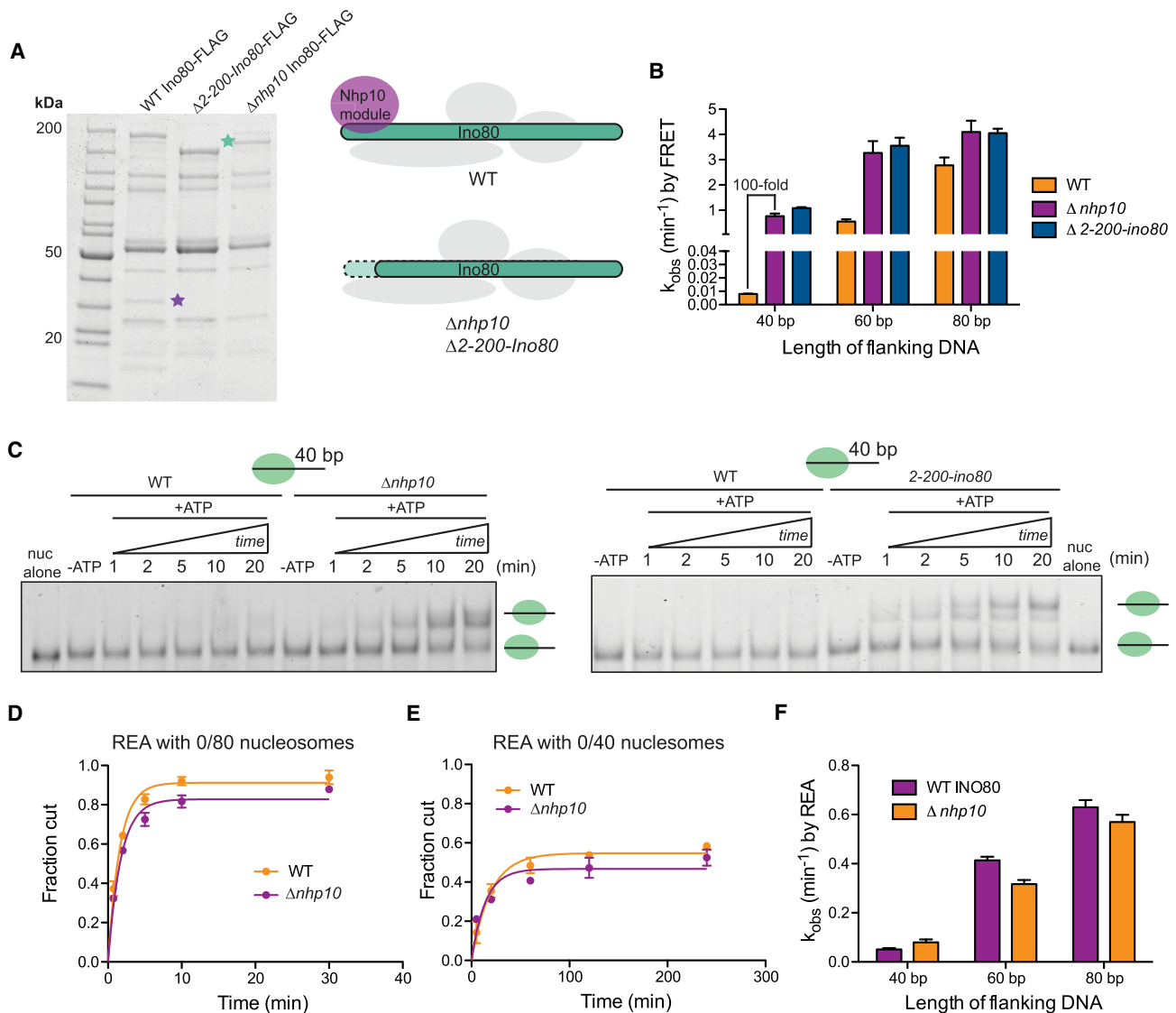


Figure 4. Deletion of *nhp10* Results in Impaired DNA Length Sensing by INO80

(A) Left: denaturing SDS-PAGE gels showing purifications of Ino80-FLAG(WT), Ino80-FLAG($\Delta 2-200$ -ino80), and Ino80-FLAG($\Delta nhp10$). Green and purple stars represent where the Ino80 ATPase and les3 (a major component of the Nhp10 module) run on the gel, respectively. Right: schematic illustrates the compositions of mutant INO80 complexes purified from $\Delta nhp10$ and $\Delta 2-200$ -ino80 strains.

(B) Remodeling rate constants measured by ensemble FRET for 0/40, 0/60, and 0/80 nucleosomes and the various INO80 mutants described in (A). These assays were performed under single-turnover conditions and with saturating enzyme and ATP.

(C) Native gel remodeling of 0/40 nucleosomes by INO80($\Delta nhp10$) and INO80($\Delta 2-200$ -ino80). These assays were performed under single-turnover conditions and with saturating enzyme and ATP. Gel remodeling of 0/60 and 0/80 nucleosomes are shown in Figure S5.

(D) Quantification of fraction cut by REA on 0/80 nucleosomes, with either INO80(WT) or INO80($\Delta nhp10$).

(E) Same as (D) but with 0/40 nucleosomes. For 0/60 nucleosomes, see Figure S5. Note difference in x axis from (D).

(F) Rate constants measured by REA for 0/40, 0/60, and 0/80 nucleosomes with INO80(WT) or INO80($\Delta nhp10$). These assays were performed under single-turnover conditions and with saturating enzyme and ATP.

Data in (B) and (F) represent means \pm SEM for three replicates.

0/60 and 0/80 nucleosomes increased by only ~ 3 -fold and ~ 1.3 -fold, respectively, with the mutant complexes (Figure 4B). Similarly, by native gel, we observed the generation of a more centered product with 0/40 nucleosomes and INO80($\Delta 2-200$ -ino80) or INO80($\Delta nhp10$), suggesting that the low-FRET product

formed by INO80($\Delta 2-200$ -ino80) and INO80($\Delta nhp10$) is indeed a slid nucleosome (Figure 4C). In addition, the final distribution of products generated from 0/60 and 0/80 nucleosomes by the mutant INO80 complexes was similar to that generated by WT INO80, consistent with the results of the FRET-based assay

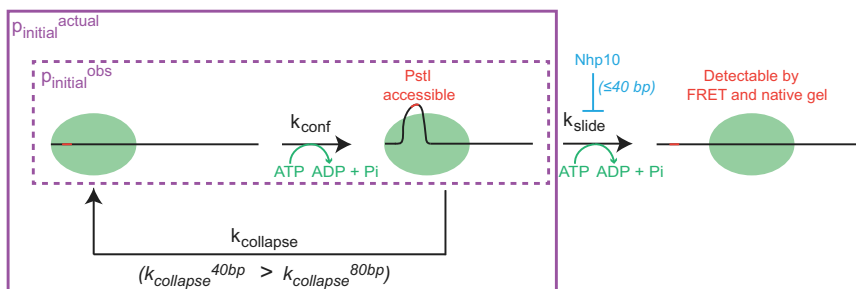


Figure 5. Model for the Length-Dependent Regulation of Sliding by INO80

Dashed purple box indicates the steps in the reaction detected by smFRET under continuous laser illumination ($p_{\text{initial}}^{\text{obs}}$). Solid purple box indicates $p_{\text{initial}}^{\text{actual}}$, which encompasses all of the events that precede translocation in our model, including the length-sensitive k_{collapse} pathway that is too slow to be detected by smFRET under continuous laser illumination. For simplicity, we have shown the Nhp10 module to only inhibit k_{slide} (see also the Discussion).

(Figures 4C and S5). Taken together, these results suggest that either the Nhp10 module or the N terminus of Ino80 is auto-inhibitory for remodeling nucleosomes with 40 bp of flanking DNA.

Comparing the remodeling rates measured by FRET versus REA with WT INO80 revealed a 25-fold difference in flanking DNA length discrimination. This comparison led us to hypothesize that overall nucleosome sliding is more sensitive to flanking DNA length than the generation and maintenance of the REA-sensitive intermediate. To further test this hypothesis, we measured remodeling rate constants by REA for INO80($\Delta nhp10$) on 0/40, 0/60, and 0/80 nucleosomes. Surprisingly, we found no significant difference in remodeling rates by REA between WT and INO80($\Delta nhp10$) for any of the nucleosome substrates (Figures 4D–4F and S5). This result was in contrast to the 100-fold increase observed by FRET for sliding 0/40 nucleosomes, and it was consistent with our hypothesis that generation of the REA-sensitive intermediate and nucleosome sliding happen in distinct kinetic steps. These data also suggest that the inhibition of sliding of nucleosomes with ≤ 40 bp of flanking DNA occurs at a step after generation of the REA intermediate (see the Discussion).

DISCUSSION

Compared to chromatin-remodeling complexes from other families, such as ISWI and SWI/SNF, the biophysical mechanism of INO80 is less well understood. In particular, while flanking DNA length has been identified as a key substrate cue in the nucleosome-sliding reaction by INO80, the mechanism behind coupling of this cue to nucleosome movement has been unclear (Udugama et al., 2011; Willhoft et al., 2017). Our study uses a complementary set of single-molecule and ensemble assays, providing a starting point for building a kinetic model for how INO80 preferentially slides nucleosomes with longer flanking DNA lengths.

Toward assembling this model, we first summarize three key findings: (1) by ensemble FRET, increasing the flanking DNA length from 40 to 80 bp results in a switch-like increase in remodeling rates, with the greatest increase (~ 100 -fold) occurring between 40 and 60 bp and a smaller (~ 3 -fold) but reproducible increase occurring between 60 and 80 bp (Figure 1C); (2) by an REA assay, nucleosomes with 40-bp flanking DNA are remodeled 10-fold faster than by ensemble FRET, and flanking DNA length regulates DNA accessibility by only 12-fold compared to the 300-fold effect observed for sliding (Figure 1G); and (3) once translocation has been initiated, flanking DNA length

does not affect either the translocation rate measured by smFRET or any pause durations within at least the first 20 bp that the nucleosome is moved (Figures 2D, 2E, and S3).

Based on these data, we propose the following model for how INO80 couples flanking DNA length sensing and nucleosome movement (Figure 5). After the addition of ATP, an intermediate that is detectable by REA is formed, a process to which we assign a rate constant k_{conf} . This intermediate can either collapse (k_{collapse}) back to its original structure or be slid (k_{slide}). Two steps in this model are regulated by flanking DNA length: k_{collapse} and k_{slide} . We propose that k_{collapse} represents the primary DNA length-sensitive step of INO80, such that k_{collapse} increases with decreasing flanking DNA length. Thus, nucleosomes with 40 bp of flanking DNA will more often collapse back to their original structure than nucleosomes with 80 bp of flanking DNA. We propose further that the Nhp10 module imposes a secondary DNA length-sensing mechanism by modulating k_{slide} for substrates with flanking DNA between 40 and 60 bp. We discuss below how this branching pathway explains the two kinetically distinct populations we observe by smFRET.

A prediction of our model in Figure 5 is that the generation of an REA-sensitive nucleosome (k_{conf}) occurs independently of sliding (k_{slide}). Consistent with this prediction, INO80($\Delta nhp10$) increases the sliding rate of nucleosomes with 40 bp of flanking DNA by 100-fold, but it increases the rate of cutting observed by REA on 0/40 nucleosomes less than 2-fold compared to WT (Figure 4). This result most simply suggests that the Nhp10 module or the N terminus of Ino80 primarily regulates length-sensitive sliding by altering k_{slide} . However, we cannot rule out the possibility that this module has small effects on k_{collapse} . We note in particular that the difference in REA between 0/40 and 0/80 nucleosomes is comparable between the INO80($\Delta nhp10$) mutant and WT (Figure 4F), consistent with our model that Nhp10 primarily affects k_{slide} .

In our model, k_{conf} and k_{collapse} both contribute to the duration of the long initial pause observed by smFRET that precedes translocation. We find that, under continuous laser illumination, the duration of this initial pause, which we call $p_{\text{initial}}^{\text{obs}}$, is ATP dependent, but not sensitive to flanking DNA lengths between 60 and 80 bp (Figures 2D and 2E). According to our model, the ATP dependence of $p_{\text{initial}}^{\text{obs}}$ comes from the ATP-dependent generation of the REA-accessible intermediate. Our model further predicts that k_{collapse} should contribute a sensitivity to flanking DNA lengths between 60 and 80 bp. However, we argue that the collapse pathway is relatively slow compared to the

photobleaching process in smFRET, so $p_{\text{initial}}^{\text{obs}}$ appears length insensitive because it captures primarily those nucleosomes that go directly to the k_{slide} pathway. Our experiment with the imaging laser off for 5 min (Figure 2H) suggests that, if we could watch nucleosomes remodel in the absence of photobleaching, the duration of this real initial pause, $p_{\text{initial}}^{\text{actual}}$, would be both ATP and DNA length dependent, because it would capture nucleosomes that go through the length-sensitive collapse pathway and re-enter the k_{conf} pathway, as well as those that go directly to k_{slide} .

This model for flanking DNA length sensing represents a significant departure from the paradigm of the better studied, DNA length-sensitive ISWI family remodelers. Our smFRET results also highlight another significant difference from the ISWI paradigm: the lack of a regulatory, substrate cue-sensitive pause that interrupts translocation after the nucleosome has moved only a short distance ($\sim 3\text{--}7$ bp) (Blosser et al., 2009; Deindl et al., 2013; Hwang et al., 2014). In contrast, once translocation is initiated, INO80 moves a nucleosome quickly (~ 7 bp/s) by at least 20 bp, without a re-assessment of flanking DNA length (Figures 2 and S3). This ability to rapidly slide a nucleosome a significant distance could be important for INO80's roles in DNA damage repair, perhaps by allowing INO80 to clear nucleosomes quickly from sites of DNA damage. This rapid sliding could also be critical for maintaining the +1 position of the nucleosome at transcription start sites, where INO80 appears to have a specialized role (Krietenstein et al., 2016).

Given how quickly and how far INO80 is capable of moving a nucleosome once sliding is initiated, it is perhaps unsurprising that the initiation of translocation is gated by two flanking DNA length-sensitive steps (Figure 5). We still do not know, however, how the translocation phase itself is regulated. Does translocation continue until the nucleosome has been moved a certain distance, greater than 20 bp? Or is the end of translocation, similar to its initiation, regulated by the length of the DNA flanking the nucleosome? A model was recently proposed for human INO80 in which ATPase activity becomes gradually uncoupled from sliding as the nucleosome reaches the center of a DNA, such that the nucleosome slows to a stop as the midpoint is reached (Willhoft et al., 2017). Our single-molecule data are inconsistent with a gradual uncoupling model, as we do not detect any changes in translocation rate that are dependent on nucleosome position, regardless of the initial position. We look forward to future work identifying the regulatory cues that end INO80's rapid translocation phase and that lead to the processive, bi-directional translocation we observe on sufficiently long DNAs like the 78/78 construct.

As noted above, the Nhp10 module specifically inhibits sliding of 0/40 nucleosomes. This inhibitory mechanism imposes a switch-like response on INO80's sliding activity for substrates with flanking DNA between 40 and 60 bp. Interestingly, Nhp10 is not found in humans, but human INO80 does contain several metazoan-specific subunits that also bind to the N terminus of the Ino80 ATPase (Chen et al., 2011). Indeed, a core complex of human INO80 lacking these N-terminal subunits does not exhibit the switch-like behavior as a function of DNA length that we observe with yeast INO80 (Willhoft et al., 2017). Rather than a 100-fold increase in overall remodeling rate constant between nucleosomes with 40- and 60-bp flanking DNA, the core

human INO80 complex exhibits a gradual increase in remodeling rate between 20- and 80-bp flanking DNA—in particular, only a 5-fold increase between 40- and 60-bp flanking DNA (Willhoft et al., 2017). While the sensitivity to flanking DNA length has not yet been tested for the complete human INO80 complex, this observation raises the possibility that there exist human INO80 subunits that play a similar role to that of the Nhp10 module in yeast.

Auto-inhibitory motifs have been discovered in several chromatin-remodeling enzymes. For example, the chromodomains of CHD1 have been shown to inhibit ATPase activity (Hauk et al., 2010), while the AutoN motif of ISWI inhibits both ATPase and remodeling (Clapier and Cairns, 2012). Both of these mechanisms are distinct from that observed for the Nhp10 module, which only inhibits remodeling of nucleosomes with short flanking DNA (Figure 4) and has no effect on ATPase rates (Tosi et al., 2013). More similar to Nhp10 is the NegC module of ISWI, which has been shown to regulate the remodeling activity of the human ISWI ATPase subunit SNF2h in a DNA length-dependent manner, with the strongest inhibitory effect (10-fold) on nucleosomes without flanking DNA (Leonard and Narlikar, 2015). An important distinction between NegC and Nhp10 is that Nhp10 exists as a separate polypeptide from the remodeling ATPase, suggesting that the presence of this module in any given INO80 complex is a potential source of regulation *in vivo*. Such differential regulation based on subunit composition has already been demonstrated for a positive regulator of INO80, the Arp5/Ies6 module, which has been shown for yeast INO80 to be required for both ATPase and remodeling activity (Chen et al., 2013; Yao et al., 2016). *In vivo*, the most highly transcribed genes also contain more Arp5, suggesting that different levels of Arp5/Ies6 may have different effects on promoter architecture (Yao et al., 2016). Our data with INO80($\Delta nhp10$) suggest that the Nhp10 module may act analogously, perhaps providing a means to regulate nucleosome sliding at sites of DNA damage. Our study, in combination with previous work on INO80, demonstrates how remodeling activity can be tuned by subunit composition, and we speculate that such tunability is important to meet the varying chromatin-remodeling needs in different genomic contexts.

STAR★METHODS

Detailed methods are provided in the online version of this paper and include the following:

- KEY RESOURCES TABLE
- CONTACT FOR REAGENT AND RESOURCE SHARING
- EXPERIMENTAL MODEL AND SUBJECT DETAILS
 - Yeast strains
- METHOD DETAILS
 - Purification of INO80 complexes from yeast
 - Mass spectrometry of INO80 complexes
 - Nucleosome labeling and reconstitution
 - Native gel remodeling assay
 - ATPase assay
 - Restriction enzyme accessibility (REA) assays
 - Ensemble FRET remodeling assay
 - Single molecule FRET measurements

- **QUANTIFICATION AND STATISTICAL ANALYSIS**
 - Error estimation for ensemble measurements
 - Hidden Markov model (HMM) analysis for extracting pause durations and FRET values from smFRET data
 - Quantification of translocation rates observed by smFRET
- **DATA AND SOFTWARE AVAILABILITY**

SUPPLEMENTAL INFORMATION

Supplemental Information includes five figures and six data files and can be found with this article online at <https://doi.org/10.1016/j.molcel.2018.01.028>.

ACKNOWLEDGMENTS

We thank Julia Tretyakova for histone purifications and the Narlikar lab for helpful discussions. We thank Toshio Tsukiyama for the yeast plasmids to make the *Δnhp10* strain and Hua-Ying Fan and Robert Kingston for plasmids containing PstI sites at 55, 94, and 118 bp in the nucleosome core. We thank Michael Stone for advice on setting up the smFRET assay. This work was supported by grants from the NIH to G.J.N. (R01GM073767) and A.J.M. (5R35GM119580), by a Ruth L. Kirschstein National Research Service Award (5F31CA180651) to C.Y.Z., and by a Leukemia and Lymphoma Society Career Development Program Fellow award to S.L.J.

AUTHOR CONTRIBUTIONS

Conceptualization, C.Y.Z., S.L.J., L.J.L., and G.J.N.; Methodology, C.Y.Z., S.L.J., L.J.L., and G.J.N.; Software, S.L.J. and M.J.J.; Investigation, C.Y.Z., S.L.J., L.J.L., and A.D.L.; Resources, S.L.B. and A.J.M.; Writing – Original Draft, C.Y.Z., S.L.J., and G.J.N.; Writing – Review & Editing, C.Y.Z., S.L.J., L.J.L., A.D.L., S.L.B., A.J.M., and G.J.N.; Supervision, G.J.N.

DECLARATION OF INTERESTS

The authors declare no competing interests.

Received: July 6, 2017

Revised: December 1, 2017

Accepted: January 22, 2018

Published: February 15, 2018

SUPPORTING CITATIONS

The following references appear in the Supplemental Information: Bondarenko et al. (2006); Brahma et al. (2017); Fan et al. (2003); Gaykalova et al. (2015); Lorch et al. (1998); Papamichos-Chronakis et al. (2011); Schnitzler et al. (1998); Shukla et al. (2010); Watanabe et al. (2013).

REFERENCES

Blosser, T.R., Yang, J.G., Stone, M.D., Narlikar, G.J., and Zhuang, X. (2009). Dynamics of nucleosome remodelling by individual ACF complexes. *Nature* **462**, 1022–1027.

Bondarenko, V.A., Steele, L.M., Újvári, A., Gaykalova, D.A., Kulaeva, O.I., Polikanov, Y.S., Luse, D.S., and Studitsky, V.M. (2006). Nucleosomes can form a polar barrier to transcript elongation by RNA polymerase II. *Mol. Cell* **24**, 469–479.

Brahma, S., Udugama, M.I., Kim, J., Hada, A., Bhardwaj, S.K., Hailu, S.G., Lee, T.-H., and Bartholomew, B. (2017). INO80 exchanges H2A.Z for H2A by translocating on DNA proximal to histone dimers. *Nat. Commun.* **8**, 15616.

Bronson, J.E., Fei, J., Hofman, J.M., Gonzalez, R.L., Jr., and Wiggins, C.H. (2009). Learning rates and states from biophysical time series: a Bayesian approach to model selection and single-molecule FRET data. *Biophys. J.* **97**, 3196–3205.

Chen, L., Cai, Y., Jin, J., Florens, L., Swanson, S.K., Washburn, M.P., Conaway, J.W., and Conaway, R.C. (2011). Subunit organization of the human INO80 chromatin remodeling complex: an evolutionarily conserved core complex catalyzes ATP-dependent nucleosome remodeling. *J. Biol. Chem.* **286**, 11283–11289.

Chen, L., Conaway, R.C., and Conaway, J.W. (2013). Multiple modes of regulation of the human Ino80 SNF2 ATPase by subunits of the INO80 chromatin-remodeling complex. *Proc. Natl. Acad. Sci. USA* **110**, 20497–20502.

Clapier, C.R., and Cairns, B.R. (2009). The biology of chromatin remodeling complexes. *Annu. Rev. Biochem.* **78**, 273–304.

Clapier, C.R., and Cairns, B.R. (2012). Regulation of ISWI involves inhibitory modules antagonized by nucleosomal epitopes. *Nature* **492**, 280–284.

Deindl, S., Hwang, W.L., Hota, S.K., Blosser, T.R., Prasad, P., Bartholomew, B., and Zhuang, X. (2013). ISWI remodelers slide nucleosomes with coordinated multi-base-pair entry steps and single-base-pair exit steps. *Cell* **152**, 442–452.

Edelstein, A.D., Tsuchida, M.A., Amodaj, N., Pinkard, H., Vale, R.D., and Stuurman, N. (2014). Advanced methods of microscope control using μ Manager software. *J. Biol. Methods* **1**, e10.

Fan, H.-Y., He, X., Kingston, R.E., and Narlikar, G.J. (2003). Distinct strategies to make nucleosomal DNA accessible. *Mol. Cell* **11**, 1311–1322.

Gaykalova, D.A., Kulaeva, O.I., Volokh, O., Shaytan, A.K., Hsieh, F.-K., Kirpichnikov, M.P., Sokolova, O.S., and Studitsky, V.M. (2015). Structural analysis of nucleosomal barrier to transcription. *Proc. Natl. Acad. Sci. USA* **112**, E5787–E5795.

Güldener, U., Heck, S., Fielder, T., Beinhauer, J., and Hegemann, J.H. (1996). A new efficient gene disruption cassette for repeated use in budding yeast. *Nucleic Acids Res.* **24**, 2519–2524.

Hall, M.A., Shundrovsky, A., Bai, L., Fulbright, R.M., Lis, J.T., and Wang, M.D. (2009). High-resolution dynamic mapping of histone-DNA interactions in a nucleosome. *Nat. Struct. Mol. Biol.* **16**, 124–129.

Harada, B.T., Hwang, W.L., Deindl, S., Chatterjee, N., Bartholomew, B., and Zhuang, X. (2016). Stepwise nucleosome translocation by RSC remodeling complexes. *eLife* **5**, 3653.

Hauk, G., McKnight, J.N., Nodelman, I.M., and Bowman, G.D. (2010). The chromodomains of the Chd1 chromatin remodeler regulate DNA access to the ATPase motor. *Mol. Cell* **39**, 711–723.

He, X., Fan, H.-Y., Narlikar, G.J., and Kingston, R.E. (2006). Human ACF1 alters the remodeling strategy of SNF2h. *J. Biol. Chem.* **281**, 28636–28647.

Hwang, W.L., Deindl, S., Harada, B.T., and Zhuang, X. (2014). Histone H4 tail mediates allosteric regulation of nucleosome remodelling by linker DNA. *Nature* **512**, 213–217.

Krietenstein, N., Wal, M., Watanabe, S., Park, B., Peterson, C.L., Pugh, B.F., and Korber, P. (2016). Genomic nucleosome organization reconstituted with pure proteins. *Cell* **167**, 709–721, e12.

Leonard, J.D., and Narlikar, G.J. (2015). A nucleotide-driven switch regulates flanking DNA length sensing by a dimeric chromatin remodeler. *Mol. Cell* **57**, 850–859.

Lorch, Y., Cairns, B.R., Zhang, M., and Kornberg, R.D. (1998). Activated RSC-nucleosome complex and persistently altered form of the nucleosome. *Cell* **94**, 29–34.

Lowary, P.T., and Widom, J. (1998). New DNA sequence rules for high affinity binding to histone octamer and sequence-directed nucleosome positioning. *J. Mol. Biol.* **276**, 19–42.

Luger, K., Mäder, A.W., Richmond, R.K., Sargent, D.F., and Richmond, T.J. (1997). Crystal structure of the nucleosome core particle at 2.8 Å resolution. *Nature* **389**, 251–260.

Luger, K., Rechsteiner, T.J., and Richmond, T.J. (1999). Preparation of nucleosome core particle from recombinant histones. *Methods Enzymol.* **304**, 3–19.

Morrison, A.J., and Shen, X. (2009). Chromatin remodelling beyond transcription: the INO80 and SWR1 complexes. *Nat. Rev. Mol. Cell Biol.* **10**, 373–384.

- Murphy, M.C., Rasnik, I., Cheng, W., Lohman, T.M., and Ha, T. (2004). Probing single-stranded DNA conformational flexibility using fluorescence spectroscopy. *Biophys. J.* **86**, 2530–2537.
- Narlikar, G.J., Phelan, M.L., and Kingston, R.E. (2001). Generation and interconversion of multiple distinct nucleosomal states as a mechanism for catalyzing chromatin fluidity. *Mol. Cell* **8**, 1219–1230.
- Papamichos-Chronakis, M., Watanabe, S., Rando, O.J., and Peterson, C.L. (2011). Global regulation of H2A.Z localization by the INO80 chromatin-remodeling enzyme is essential for genome integrity. *Cell* **144**, 200–213.
- Partensky, P.D., and Narlikar, G.J. (2009). Chromatin remodelers act globally, sequence positions nucleosomes locally. *J. Mol. Biol.* **397**, 12–25.
- Polach, K.J., and Widom, J. (1995). Mechanism of protein access to specific DNA sequences in chromatin: a dynamic equilibrium model for gene regulation. *J. Mol. Biol.* **254**, 130–149.
- Schnitzler, G., Sif, S., and Kingston, R.E. (1998). Human SWI/SNF interconverts a nucleosome between its base state and a stable remodeled state. *Cell* **94**, 17–27.
- Shen, X. (2004). Preparation and analysis of the INO80 complex. *Methods Enzymol.* **377**, 401–412.
- Shen, X., Mizuguchi, G., Hamiche, A., and Wu, C. (2000). A chromatin remodeling complex involved in transcription and DNA processing. *Nature* **406**, 541–544.
- Shen, X., Ranallo, R., Choi, E., and Wu, C. (2003a). Involvement of actin-related proteins in ATP-dependent chromatin remodeling. *Mol. Cell* **12**, 147–155.
- Shen, X., Xiao, H., Ranallo, R., Wu, W.-H., and Wu, C. (2003b). Modulation of ATP-dependent chromatin-remodeling complexes by inositol polyphosphates. *Science* **299**, 112–114.
- Shukla, M.S., Syed, S.H., Montel, F., Faivre-Moskalenko, C., Bednar, J., Travers, A., Angelov, D., and Dimitrov, S. (2010). Remosomes: RSC generated non-mobilized particles with approximately 180 bp DNA loosely associated with the histone octamer. *Proc. Natl. Acad. Sci. USA* **107**, 1936–1941.
- Stryer, L., and Haugland, R.P. (1967). Energy transfer: a spectroscopic ruler. *Proc. Natl. Acad. Sci. USA* **58**, 719–726.
- Tosi, A., Haas, C., Herzog, F., Gilmozzi, A., Berninghausen, O., Ungewickell, C., Gerhold, C.B., Lakomek, K., Aebersold, R., Beckmann, R., and Hopfner, K.P. (2013). Structure and subunit topology of the INO80 chromatin remodeler and its nucleosome complex. *Cell* **154**, 1207–1219.
- Udugama, M., Sabri, A., and Bartholomew, B. (2011). The INO80 ATP-dependent chromatin remodeling complex is a nucleosome spacing factor. *Mol. Cell Biol.* **31**, 662–673.
- Watanabe, S., Radman-Livaja, M., Rando, O.J., and Peterson, C.L. (2013). A histone acetylation switch regulates H2A.Z deposition by the SWR-C remodeling enzyme. *Science* **340**, 195–199.
- Whitehouse, I., Stockdale, C., Flaus, A., Szczelkun, M.D., and Owen-Hughes, T. (2003). Evidence for DNA translocation by the ISWI chromatin-remodeling enzyme. *Mol. Cell Biol.* **23**, 1935–1945.
- Willhoft, O., McCormack, E.A., Aramayo, R.J., Bythell-Douglas, R., Ocloo, L., Zhang, X., and Wigley, D.B. (2017). Crosstalk within a functional INO80 complex dimer regulates nucleosome sliding. *eLife* **6**, e25782.
- Wolffe, A.P., Jordan, E., and Brown, D.D. (1986). A bacteriophage RNA polymerase transcribes through a *Xenopus* 5S RNA gene transcription complex without disrupting it. *Cell* **44**, 381–389.
- Yang, J.G., Madrid, T.S., Sevastopoulos, E., and Narlikar, G.J. (2006). The chromatin-remodeling enzyme ACF is an ATP-dependent DNA length sensor that regulates nucleosome spacing. *Nat. Struct. Mol. Biol.* **13**, 1078–1083.
- Yao, W., King, D.A., Beckwith, S.L., Gowans, G.J., Yen, K., Zhou, C., and Morrison, A.J. (2016). The INO80 complex requires the Arp5-les6 subcomplex for chromatin remodeling and metabolic regulation. *Mol. Cell Biol.* **36**, 979–991.
- Yen, K., Vinayachandran, V., Batta, K., Koerber, R.T., and Pugh, B.F. (2012). Genome-wide nucleosome specificity and directionality of chromatin remodelers. *Cell* **149**, 1461–1473.
- Yen, K., Vinayachandran, V., and Pugh, B.F. (2013). SWR-C and INO80 chromatin remodelers recognize nucleosome-free regions near +1 nucleosomes. *Cell* **154**, 1246–1256.
- Zhang, Z., Wippo, C.J., Wal, M., Ward, E., Korber, P., and Pugh, B.F. (2011). A packing mechanism for nucleosome organization reconstituted across a eukaryotic genome. *Science* **332**, 977–980.
- Zhou, C.Y., and Narlikar, G.J. (2016). Analysis of nucleosome sliding by ATP-dependent chromatin remodeling enzymes. *Methods Enzymol.* **573**, 119–135.
- Zhou, C.Y., Johnson, S.L., Gamarra, N.I., and Narlikar, G.J. (2016). Mechanisms of ATP-dependent chromatin remodeling motors. *Annu. Rev. Biophys.* **45**, 153–181.
- Zofall, M., Persinger, J., and Bartholomew, B. (2004). Functional role of extra-nucleosomal DNA and the entry site of the nucleosome in chromatin remodeling by ISW2. *Mol. Cell Biol.* **24**, 10047–10057.

STAR★METHODS

KEY RESOURCES TABLE

REAGENT or RESOURCE	SOURCE	IDENTIFIER
Antibodies		
Rabbit polyclonal anti-FLAG	Sigma-Aldrich	F7425; RRID: AB_439687
Chemicals, Peptides, and Recombinant Proteins		
ATP	GE Healthcare	27-2056-01
Pst1	NEB	R0140
γ - ³² P-ATP	Perkin Elmer	Blu002Z250uC
N-(2-aminoethyl)-3-aminopropyltrimethoxysilane	United Chemicals	A0700
mPEG-SVA	Laysan Bio	N/A
biotin-PEG-SVA	Laysan Bio	N/A
acetylated BSA	Promega	R3691
Trolox	Sigma	238813
Catalase	Sigma	E3289
Glucose oxidase	Sigma	G2133
Experimental Models: Organisms/Strains		
<i>S. cerevisiae</i> : INO80-FLAG: s288c INO80-FLAG	Shen, 2004	N/A
<i>S. cerevisiae</i> : INO80-FLAG(Δ nhp10): s288c INO80-FLAG Δ nhp10::KanMX	This paper	N/A
<i>S. cerevisiae</i> : INO80-FLAG(Δ 2-200-ino80): s288c Δ 2-200-ino80-FLAG::NAT	This paper	N/A
Oligonucleotides		
0/100 601 DNA sequence	This paper	N/A
CTGGAGAATCCCGGTGCCGAGGCCGCTCAATTGGTCGTAGACAGCTCTA GCACCGCTTAAACGCACGTACGCGCTGTCCCCGCGTTTTAACCGCCAA GGGGATTACTCCCTAGTCTCCAGGCACGTGTCAGATATATACATCCTGTG CATGTATTGAACAGCGACCTTGCCGGTGCCAGTCGGATAGTGTCCGAG CTCCACTCTAGAGGATCCCCGGGTACCGAGCTCGAATTCGCCCTATA		
78/78 601 DNA sequence (base with Cy5 enclosed by asterisks)	This paper	N/A
GGATCCTAATGACCAAGGAAAGCATGATTCTCACACCGAGTTCATCCCT TATGTGATGGACCCCTATAC*T*CGGCCGCCCTGGAGAATCCCGGTCTGCA GGCCGCTCAATTGGTCGTAGACAGCTCTAGCACCGCTTAAACGCACGTA CGCGCTGTCCCCGCGTTTTAACCGCCAAGGGGATTACTCCCTAGTCTC CAGGCACGTGTCAGATATATACATCCTGTGCATCTATTGAACAGCGACCTT GCCGGTGCCAGTCGGATAGTGTCCGAGCTCCCACTCTAGAGGATCCCC GGT ACC		
0/80 5S DNA sequence	This paper	N/A
GGCCCGACCCTGCTTGGCTGCAGAGATCAGACGATATCGGGCACTTTCA GGTGGTATGGCCGTAGCGGAGCACAAGGCTGACTTTTCCCTCCCTTGT GCTGCCTTCTGGGGGGGGCCAGCCGGATCCCCGGGCGAGCTCGAATT CGTAATCATGTCATAGCTGTTTCTGTGTGAAATTGTTATCCGCTCACAAT TCCACACAACATACGAGCCGGAAGCATAA		
0/80 601 Pst1-18 (Pst1 site is bolded)	This paper	N/A
CTGGAGAATCCCGGT CTGCAG GCCGCTCAATTGGTCGTAGACAGCTCTA GCACCGCTTAAACGCACGTACGCGCTGTCCCCGCGTTTTAACCGCCAA GGGGATTACTCCCTAGTCTCCAGGCACGTGTCAGATATATACATCCTGTG CATGTATTGAACAGCGACCTTGCCGGTGCCAGTCGGATAGTGTCCGAGC TCCCACTCTAGAGGATCCCCGGGTACCGA		

(Continued on next page)

Continued

REAGENT or RESOURCE	SOURCE	IDENTIFIER
0/40 601 Pst1-55 (Pst1 site is bolded) CTGGAGAATCCCGGTCTGCAGGCCGCTCAATTGGTCGTAGACAGCTCTA GCC CTGCAG TAAACGCACGTACGCGCTGTCCCCCGCGTTTTAACCGCAA GGGGATTACTCCCTAGTCTCCAGGCACGTGCAGATATACATCCTGTG CATGTATTGAACAGCGACCTTGCCGGTGCCAGTCGGATA	This paper	N/A
0/40 601 Pst1-94 (Pst1 site is bolded) CTGGAGAATCCCGGTCTGCAGGCCGCTCAATTGGTCGTAGACAGCTC TAGCCTGCAGTAAACGCACGTACGCGCTGTCCCCCGCGTTTT CTGCAG CAAGGGGATTACTCCCTAGTCTCCAGGCACGTGCAGATATACATCC TGTGCATGTATTGAACAGCGACCTTGCCGGTGCCAGTCGGATA	This paper	N/A
0/40 601 Pst1-118 (Pst1 site is bolded) CTGGAGAATCCCGGTCTGCAGGCCGCTCAATTGGTCGTAGACAGCTC TAGCCTGCAGTAAACGCACGTACGCGCTGTCCCCCGCGTTTTCTGCAG CAAGGGGATTACTCCCTA CTGCAG AGGCACGTGCAGATATACATC CTGTGCATGTATTGAACAGCGACCTTGCCGGTGCCAGTCGGATA	This paper	N/A
See also Data S1 .	N/A	N/A
Recombinant DNA		
pUG6 plasmid	Güldener et al., 1996	N/A
601 plasmid	Lowary and Widom, 1998	N/A
5S plasmid	This paper	N/A
601_Pst55 plasmid	He et al., 2006	N/A
601_Pst94 plasmid	He et al., 2006	N/A
601_Pst118 plasmid	He et al., 2006	N/A
Pet3a_H2A (<i>Xenopus laevis</i>)	Yang et al., 2006	N/A
Pet3a_H2B (<i>Xenopus laevis</i>)	Yang et al., 2006	N/A
Pet3a_H3 (<i>Xenopus laevis</i>)	Yang et al., 2006	N/A
Pet3a_H4 (<i>Xenopus laevis</i>)	Yang et al., 2006	N/A
Software and Algorithms		
Scaffold 4	Proteome Software	https://www.proteomesoftware.com/products/scaffold/
Graphpad Prism 5	Graphing and modeling software	https://www.graphpad.com
Micro-Manager	Microscopy image acquisition software	https://micro-manager.org/
Traces	Single molecule FRET analysis software	https://github.com/stephij/Traces
pyhsmm	HMM analysis software	https://github.com/mattjj/pyhsmm
Slopey	Continuous-time hidden semi Markov model for smFRET data	https://github.com/stephij/slopey

CONTACT FOR REAGENT AND RESOURCE SHARING

Further information and requests for resources and reagents should be directed to and will be fulfilled by the Lead Contact, Geeta J. Narlikar (geeta.narlikar@ucsf.edu).

EXPERIMENTAL MODEL AND SUBJECT DETAILS**Yeast strains**

All yeast used for protein purification were grown at 30 degrees. For all of the experiments using wild-type INO80, yeast were first inoculated in YPD from a frozen glycerol stock and then transferred into SC media. The yeast were then grown until saturation, 50 g/liter of YPD powder was added, and cells were harvested six hours later. For experiments involving mutants of INO80, yeast

were grown only in YPD and harvested upon saturation. We tested the activity of wild-type INO80 purified using either of these growth protocols and found no difference.

METHOD DETAILS

Purification of INO80 complexes from yeast

INO80 was purified by FLAG immunoprecipitation based on previously published methods (Shen, 2004). Briefly, *S. cerevisiae* with endogenously FLAG-tagged INO80 (Shen, 2004) was grown in YEPD at 30°C to saturation. Cells were pelleted by centrifugation for 10 min at 5000 rpm, resuspended with buffer H0.3 (25 mM HEPES, pH 7.5, 1 mM EDTA, pH 8.0, 10% glycerol, 0.02% NP-40, 0.3 M KCl), and pelleted again. Pelleted cells were then extruded through a 60 mL syringe into liquid nitrogen to create “noodles.” Cell “noodles” were then lysed using a Tissue Lyser II (QIAGEN, Hilden Germany) or a freezer mill (SPEX 6970 EFM), cooled in liquid nitrogen. Frozen lysate powder was resuspended in equal volume of H0.3 and spun in an SW28 rotor for 2 hr at 25,000 rpm at 4°C. Clarified lysate was mixed with equal volume buffer H0.3 and applied to FLAG M2-affinity resin (1 mL bead slurry per 40 mL of cleared lysate) equilibrated with H0.3 and incubated for 3 hours at 4°C. An additional dose of protease inhibitors was added halfway through the incubation. Resin was washed with 3x50 mL buffer H0.5 (H0.3 buffer except with 0.5 M KCl) followed by 3x10 mL washes with buffer H0.1 (0.1 M KCl) and eluted with H0.1 supplemented with 1mg/mL FLAG peptide. Eluate was concentrated, aliquoted, flash frozen in liquid nitrogen, and stored at –80°C. INO80 concentration was determined by SDS-PAGE with BSA standards, based on the intensity of the Ino80-FLAG band.

To generate the INO80(Δ 2-200-*ino80*) construct, amino acids 2-200 of Ino80 were deleted by knock-in at the endogenous locus in the Ino80-FLAG strain, using a NAT marker –700 bp upstream of the ORF. The mutation was verified by colony PCR and by sequencing. INO80(Δ *nhp10*) was made similarly except that a KanMX marker was knocked into the endogenous *Nhp10* locus. Mutant complexes were purified as described above for WT INO80.

Mass spectrometry of INO80 complexes

1.5 μ g of WT INO80 or INO80(Δ *nhp10*) were run on a 4%–20% SDS gel and stained with Colloidal Blue (Thermo Fisher Scientific, Waltham, MA). The INO80 band and the truncated band were cut out and submitted to the UC Davis Mass Spectrometry Facilities (Davis, CA) for analysis. The samples were trypsin digested and run on a Xevo G2 QToF coupled to a nanoAcquity UPLC system (Waters, Milford, MA). RAW MSe files were processed using Protein Lynx Global Server (PLGS) version 2.5.3 (Waters, Milford, MA). Sequences were searched against the *S. cerevisiae* database from uniprot.org, as well as common contaminants including human keratins, porcine trypsin, bovine serum albumin, and bovine beta-casein. Searches were performed with trypsin specificity and allowed for three missed cleavages.

Nucleosome labeling and reconstitution

Recombinant *Xenopus laevis* histones were expressed and purified from *E. coli* as previously described (Luger et al., 1999). Histone octamer was reconstituted as previously described (Luger et al., 1999; Zhou and Narlikar, 2016). FRET-labeled nucleosomes, with the donor Cy3 (for smFRET) or the acceptor Cy5 (for ensemble) on histone H3, were generated via a cysteine introduced at position 33, and were labeled prior to histone octamer assembly via cysteine-maleimide chemistry. Octamer for smFRET was assembled using a 2:1 unlabeled:labeled H3 mixture, to generate nucleosomes with mostly one H3 or neither H3 labeled; labeled octamer for ensemble FRET was assembled with all labeled histone H3. Nucleosomes for REA were not labeled on the histones. Cy3-labeled (for ensemble assays) and Cyanine 5 SE-labeled and biotinylated DNAs (for smFRET) were generated by PCR with HPLC-purified, labeled primers (Cy5 end-labeled primers: TriLink Biotechnologies, San Diego, CA; Cy5 internally labeled primers for centered constructs, IBA Life Sciences, Göttingen, Germany; Cy3 and biotinylated primers: IDT, Coralville, IA) and purified by PAGE. In most cases, nucleosomes were assembled using the 601 nucleosome positioning (Lowary and Widom, 1998). Where indicated, the naturally occurring 5S sequence from *X. borealis*, with a different arbitrary sequence in the flanking DNA, was used instead (Wolffe et al., 1986). These DNAs were assembled with either labeled or unlabeled octamers by salt gradient dialysis, purified by glycerol gradient centrifugation, and quantified by native gel (Zhou and Narlikar, 2016). DNA sequences used in this work are given in [Data S1](#).

Native gel remodeling assay

All gel remodeling reactions were performed under single turnover conditions (enzyme in excess of nucleosomes), where enzyme concentration is saturating. Saturation was determined by increasing the concentration of enzyme by 3-fold without an observable increase in the rate constant. Reactions were performed at 30°C with 10 nM FRET-labeled nucleosomes, saturating enzyme (15 nM for WT INO80, 30 nM for INO80(Δ *nhp10*) and INO80(Δ 2-200-*ino80*)), 40 mM Tris pH 7.5, 60 mM KCl, 2 mM ATP·MgCl₂, 1.1 mM MgCl₂, 0.02% NP40, 1%(v/v) glycerol, and 0.5 mg/mL FLAG peptide. Reactions were assembled without ATP-Mg²⁺ and incubated at 30°C for 10 minutes prior to the addition of ATP. At the times indicated, a small portion of the reaction was removed and quenched with excess ADP and plasmid DNA. Time points were then resolved by native PAGE (6% acrylamide, 0.5XTBE) and scanned on a Typhoon variable mode imager (GE Life Sciences, Pittsburgh, PA) by scanning for Cy3. Gels were then quantified by densitometry using ImageJ.

ATPase assay

ATPase reactions were performed under multiple turnover conditions (ATP in excess of enzyme). Reactions were performed at 30°C with 5 nM nucleosomes, 15 nM INO80, 40 mM Tris pH 7.5, 50 mM KCl, 100 mM ATP·MgCl₂, 0.5 mM MgCl₂, and trace amounts of γ -³²P-ATP. Reactions were assembled without ATP-Mg²⁺ and incubated at 30°C for 10 minutes prior to the addition of ATP. 2.5 μ L time points were quenched with an equal volume of 50 mM Tris pH 7.5, 3% SDS, and 100 mM EDTA. Inorganic phosphate was resolved from ATP on a PEI-cellulose TLC plate (Select Scientific) with 0.5 M LiCl/1M formic acid mobile phase. Plates were dried, exposed to a phosphorscreen overnight, and scanned on a Typhoon variable mode imager. Rate constants were determined by fitting a line through the first 10% of inorganic phosphate generated using Prism.

Restriction enzyme accessibility (REA) assays

With the exception of the titration experiments in Figures S2G and S2H, all REA reactions were performed under single turnover conditions (enzyme in excess of nucleosomes) and at 30°C. Enzyme concentration was also determined to be saturating using methods described previously. Final conditions were: saturating enzyme (20 nM for WT INO80, 60 nM for INO80($\Delta nhp10$)), 15 nM nucleosomes, 40 mM Tris pH 7.5, 60 mM KCl, 1 mM ATP·MgCl₂, 5 mM MgCl₂, 0.01% NP40, 0.5 mg/mL FLAG peptide, and 3 U/ μ L Pst1 (NEB). Final conditions for the titration experiments in Figures S2G and S2H were the same, except that 20 nM nucleosomes and 10 nM, 20 nM, or 40 nM WT INO80 were used. Reactions were assembled without ATP·MgCl₂ and incubated at 30°C for 15 minutes before addition of ATP. Time points were quenched with an equal volume of stop solution (70 mM EDTA, 20 mM Tris, pH 7.5-7.7, 2% SDS, 20% glycerol, 0.2 mg/ml xylene cyanole and 0.2 bromophenol blue). After all time points were completed, Proteinase K was added to each sample to a final concentration of 4 mg/mL and incubated for 20 minutes at 50°C. Time points were then resolved by native PAGE (6% acrylamide, 0.5XTBE) and scanned on a Typhoon variable mode imager (GE Life Sciences, Pittsburgh, PA). All gels were imaged by scanning for Cy3, except for the gels in Figure S2C, which were stained with SYBR Gold (S11494, Thermo Fisher Scientific, Waltham, MA). Fraction of DNA cut was quantified by densitometry using ImageJ. The data were fit to a single exponential decay using Prism 6 (GraphPad, La Jolla, CA) (Equation 1),

$$y = (y_0 - p)e^{-k_{obs} t} + p, \quad (\text{Equation 1})$$

where y_0 is the initial fraction un-cut, k_{obs} is the observed rate constant (min^{-1}), and p is the fraction DNA un-cut at plateau.

For the REA assays with the Pst18 site in the linker, the same equation was used, except that y_0 represented the initial fraction DNA cut and p is the fraction DNA cut at the plateau.

Ensemble FRET remodeling assay

For all ensemble FRET remodeling experiments except those in Figures 2F and S4E, assays were performed under the same conditions as gel remodeling assays, except that 5 nM nucleosomes were used. For the reactions in Figures 2F and S4E, 7.5 nM nucleosomes were used. Reactions were initiated by addition of ATP, and then the Cy5 emission intensity was measured every second in a K2 fluorometer (ISS) equipped with a 550 nm short pass excitation filter and a 535 nm long pass emission filter. Reactions were excited at 515 nm and emission was measured at 665 nm. The resulting curves were fit to a two-phase exponential decay (Equation 2),

$$y = p + (y_0 - p)(f_{fast} e^{-k_{fast} t} + (1 - f_{fast}) e^{-k_{slow} t}), \quad (\text{Equation 2})$$

where f_{fast} is the fraction in the fast phase and k_{fast} and k_{slow} are the remodeling rates of the fast and slow phase respectively. All rate constants reported for ensemble FRET assays (“ k_{obs} ” on figure axes) are the k_{fast} value obtained from the fit, with the exception of the ensemble FRET rate constants reported in Figures S3G and S4E. Data in Figures S3G and S4E were obtained at 20°C rather than 30°C, and so these slower data were fit to a single exponential decay, with the reported rate constant being the decay rate of the single exponential.

The data in Figure 2F represent the average of two independent remodeling reactions. Each dataset (i.e., independent replicate of Cy5 intensity over time) was down-sampled by taking the average Cy5 intensity over non-overlapping 3 s windows. Two such down-sampled replicates were then averaged to obtain each of the curves in Figure 2F.

Single molecule FRET measurements

Cleaning and PEGylation of quartz slides

GE 124 quartz slides (G. Finkenbeiner, Waltham, MA) with laser-drilled holes for tubing attachment were cleaned by sonication in a bath sonicator in 2.5% Alconox for 10 minutes, rinsed thoroughly with water, then sonicated in acetone (HPLC grade, Sigma-Aldrich) for 15 minutes followed by methanol (HPLC grade, Sigma-Aldrich) for 15 minutes. Slides were rinsed with water, and then slides and coverslips (24 mm x 50 mm, No. 1.5, VWR, Radnor, PA) were sonicated in 1 M KOH (Sigma-Aldrich) for not more than 20 minutes, followed by sonication in water for 20 minutes. A propane torch was used to burn any remaining epoxy from previous experiments off of the slides as the final cleaning step.

Slides and coverslips were silanized with a mixture of methanol (Sigma-Aldrich), glacial acetic acid (Sigma-Aldrich), and N-(2-aminoethyl)-3-aminopropyltrimethoxysilane (APTMS, United Chemicals A0700, Bristol, PA) at a volumetric ratio of 200 methanol:1

acetic acid:2 APTMES. Slides and coverslips were sonicated in this mixture for 30 s, incubated in the dark for 10 minutes, then sonicated for another 30 s and incubated for another 10 minutes. Slides and coverslips were rinsed with methanol and dried with compressed air.

A PEG mixture consisting of 32 mPEG-SVA:1 biotin-PEG-SVA (Laysan Bio, Arab, AL) by weight was diluted to 0.25 mg/ μ L in 0.1 M sodium bicarbonate and then applied to the slides and coverslips and incubated for an hour, followed by an additional incubation with 0.33 mg/ μ L mPEG alone for an additional hour. Slides and coverslips were rinsed with water, dried with compressed air, and stored in the dark under vacuum at -20°C . No deterioration in surface quality was observed even after several months under these storage conditions.

Sample preparation

PEGylated slides were brought to room temperature, and then chambers were constructed between a slide and a coverslip with double-sided tape. Thin-walled tubing (ETT-28 or ETT-26, Weico Wire and Cable, Edgewood, NY) was affixed to each chamber's input and output holes for buffer exchange. Chambers were first washed with buffer SPB (50 mM HEPES-KOH, pH 7.5 at 22°C , and 60 mM KCl), and then passivated with 0.2 mg/mL acetylated BSA (R3691, Promega, Madison, WI) in SPB. After five minutes, chambers were washed with Wash Buffer (12 mM HEPES-KOH, pH 7.5 at 22°C , 50 mM KCl, 0.52 mM MgCl_2 , 10% (v/v) glycerol, 0.6 mM EDTA, 0.02% Igepal [Sigma-Aldrich I8896], 1% [w/v] glucose, and 0.1 mg/mL acetylated BSA). Neutravidin (A2666, Thermo Fisher Scientific, Waltham, MA) at 0.2 mg/mL in Wash Buffer was then added and incubated for 5 minutes. After washing with Wash Buffer, nucleosomes at 12.5 pM in Wash Buffer were added and incubated for 10 minutes. (If necessary, serial dilutions of nucleosomes were performed in 20% glycerol gradient buffer [20 mM HEPES, pH 7.5 at 4°C , 1 mM EDTA, 20% glycerol, 0.1% Igepal]. Nucleosomes were imaged within 90 minutes of dilution into Wash Buffer.) Unbound nucleosomes were removed by washing with Wash Buffer. All incubations were at 20°C . All flow-throughs were of sufficient volume (150 μ L) to ensure complete buffer exchange in the ~ 30 μ L channels.

Data acquisition

Nucleosomes were imaged on a custom-built prism-based TIRF setup, consisting of an inverted Olympus (Burlingame, CA) 1x71 microscope with a PL APO 60x water immersion objective and an Andor (Belfast, Ireland) iXon X3 897 EMCCD camera, illuminated by a 532 nm diode-pumped solid-state laser (R531001GX, Laserglow, Toronto, ON, Canada). Light from the sample was filtered with a 577 nm/690 nm dual band-pass filter (FF01-577/690-25, Semrock, Rochester, NY), passed through an adjustable slit (VA100, Thor Labs, Newton, NJ), and split into donor and acceptor images by a 638 nm longpass dichroic mirror (Thor Labs DMLP638). The two images were focused by separate lenses (Thor Labs AC508-100-A) onto the two halves of the camera.

All smFRET experiments were performed at 20°C to extend dye lifetimes. Immediately prior to data acquisition, the sample chamber was flushed with 300 μ L of 15 nM INO80 in imaging buffer (53 mM HEPES-KOH, pH 7.5 at 22°C , 9.1 mM Tris-acetate, pH 7.5 at 22°C [contributed by the Trolox], 53 mM KCl, 0.52 mM MgCl_2 , 10% glycerol, 0.6 mM EDTA, 0.02% Igepal (Sigma CA-630), 1% [w/v] glucose, 0.1 mg/mL acetylated BSA, 2 mM Trolox [Sigma 238813, made as an 11 mM stock in Tris-acetate, pH'd to 7.5 with 1 M NaOH, and stored at 4°C], 0.03 mM β -mercaptoethanol, 2 U/ μ L catalase [= 0.2 mg/mL; Sigma E3289], and 0.08 U/ μ L glucose oxidase [0.8 mg/mL, Sigma G2133; made with the catalase as a 100x stock in SPB, and stored at 4°C for not more than one week]). INO80 was allowed to bind nucleosomes for 10 min prior to the addition of ATP. Images were collected using Micro-Manager (<https://www.micro-manager.org>, San Francisco, CA) (Edelstein et al., 2014) at 7.4 Hz, with an exposure time of 100 ms. To start each reaction, saturating ATP (1 mM) in 600 μ L imaging buffer were added via an automated syringe pump (J-KEM Scientific, St. Louis, MO). Injection times were calibrated using a flash from a 638 nm laser (Vortran Laser Technology 10567, Sacramento, CA) as a fiducial mark, combined with a measurement of the syringe pump delay (2.6 ± 0.3 s). For double-chase experiments, an additional 600 μ L of imaging buffer alone, or saturating ATP in imaging buffer, were added via syringe pump, using a flash from a 638 nm laser as a fiducial mark.

Obtaining intensity-versus-time traces from raw image data

To streamline the data analysis process for large datasets, as well as to improve the overall quality of the data, we developed custom in-house software called Traces, available for download at <https://github.com/stephij/Traces>, to analyze the raw camera images obtained by Micro-Manager. The Traces analysis pipeline is summarized in Data S2. Traces facilitates the analysis of large datasets by automating many of the analysis steps, offering computational and manual checks at each of these steps to ensure data quality, and allowing the user to save and rerun various parts of the analysis without needing to rerun all of it. Moreover, Traces includes a simple graphical user interface that allows the user to examine the original camera images alongside the calculated dye intensities and FRET values, which is instrumental in excluding spurious events. More details can be found in the manual that accompanies the Traces software.

In the example traces in Figures 2B, 3C, 3D, and S4A–S4C, traces were cropped where one of the dyes photobleached.

Microscope calibration for conversion from FRET to base pairs of DNA

Following previous smFRET studies with mononucleosomes (Blosser et al., 2009; Deindl et al., 2013), we generated a calibration curve of FRET signal as a function of exit DNA linker length, by constructing a series of nucleosomes with 78 bp between the nucleosome and the biotinylated DNA end on one side, and varying DNA lengths between the other side of the nucleosome and the Cy5-labeled DNA end (Data S4). As with the nucleosomal constructs used for remodeling in this work (see Figure S3A), KDEs and CDFs of the FRET values for most of the calibration constructs show two peaks, corresponding to nucleosomes with the Cy3-labeled H3 either proximal to or distal to the Cy5-DNA end. (As with nucleosomes used for remodeling assays, any nucleosomes with labels

on both the proximal and distal H3's are distinguishable by two-step photobleaching and are excluded.) The exceptions are the 16/78 and 25/78 constructs, for which the proximal versus distal populations have FRET values too similar to easily distinguish, such that the cdfs show only one peak.

In contrast to previous work (Blosser et al., 2009; Deindl et al., 2013), we observe a nonlinear relationship between FRET and flanking DNA length. We propose that, due to technical differences between our work and others' (e.g., choice of filter sets and other optical components, labeling of histone H3 instead of H2A), previous smFRET studies with mononucleosomes occupied a pseudo-linear range of the FRET-versus-bp relationship, which in our hands is the range from about 5 to 20 bp (Data S4C). To better capture the FRET-versus-bp relationship in our setup, we therefore derived a non-linear expression for the relationship between FRET and the length n of DNA flanking the nucleosome, as follows:

We start with the known relationship between FRET and inter-dye distance R (Stryer and Haugland, 1967),

$$\text{FRET}(R) = \frac{1}{1 + R^6/R_0^6}, \quad (\text{Equation 3})$$

where R is the inter-dye distance in three dimensions in nm and R_0 is the Förster radius for Cy3-Cy5 in nm (Murphy et al., 2004; Stryer and Haugland, 1967). We then use the law of cosines to approximate the geometric relationship between inter-dye distance and flanking DNA length n , namely, that

$$R^2 = d_0^2 + L^2 - 2d_0L \cos \theta, \quad (\text{Equation 4})$$

where L is the length of the flanking DNA in nm, d_0 is the average distance in nm between the dyes when $L = 0$, and θ is the angle between d_0 and the DNA vector (Data S4B). Given that 1 bp = 0.34 nm, $L = 0.34n$, where n is the number of bp between the Cy5-labeled DNA end and the edge of the nucleosome. Thus we can write the relationship between FRET and n as

$$\text{FRET}(n) = \frac{1}{1 + \frac{(d_0^2 + 0.1156n^2 - 0.68d_0n \cos \theta)^3}{R_0^6}}. \quad (\text{Equation 5})$$

Before commenting on the fit of this expression to our calibration data, we first make several observations about the nature of Equation 5. First, in contrast to the behavior of $\text{FRET}(R)$, $\text{FRET}(n)$ will only ever get arbitrarily close to 1, because of the finite distance between the dyes represented by d_0 . In fact, the maximal FRET value we would measure, when $n = 0$, is determined by the ratio between d_0 and R_0 ; specifically,

$$\text{FRET}(n=0) = \frac{1}{1 + (d_0/R_0)^6}. \quad (\text{Equation 6})$$

Second, also in contrast to $\text{FRET}(R)$, half-maximal FRET does not occur when $n = R_0$. Instead, the value of n that yields half-maximal FRET is controlled by all three free parameters. Specifically, half-maximal FRET occurs when

$$d_0^2 + 0.1156n^2 - 0.68d_0n \cos \theta = R_0^2. \quad (\text{Equation 7})$$

Data S5 shows the effects of each individual parameter of Equation 5 on the shape of the $\text{FRET}(n)$ curve, as well as the effect of varying d_0/R_0 . As expected, d_0/R_0 primarily controls the y-intercept of the curve, while all three parameters affect the half-maximal point. Importantly, varying the parameters of Equation 5 has the largest effects where n is small. This is fortuitous, since measuring low or zero FRET is difficult, and our assignments of proximal and distal peaks for $n \geq 20$ bp are less certain than for $n < 20$ bp.

The curves in Data S5 were generated using reasonable estimates for parameter values. In particular, the Förster radius R_0 for Cy3-Cy5 under similar conditions to ours is 6 nm (Murphy et al., 2004), and our calibration data levels off at about 0.95 FRET, so we would expect d_0 to be roughly 3.7 nm. The perpendicular distance between the Cy3 dye on the H3 tail and the proximal DNA vector in the crystal structure of the nucleosome, which we call d_{\perp} , is on the order of 2-3 nm (Luger et al., 1997), and in fact based on the crystal structure we might consider a reasonable assumption that $d_{\perp} \cong d_0$, i.e., that $\theta \approx 90^\circ$. However, the C_6 linker that attaches the Cy5 dye to the DNA end adds a length equivalent to 1-2 bp, such that even when $n = 0$, the Cy5 dye probably protrudes further from the histone octamer than the end of the DNA in the crystal structure. Therefore we might hypothesize that $\theta > 90^\circ$ and $d_0 = d_{\perp}/\sin(180^\circ - \theta)$.

We turn now to the question of fitting Equation 5 to our calibration data. We found it difficult to get a robust fit to seven calibration points with a model with three free parameters, so we took advantage of the additional information provided by the distal FRET peaks in our calibration measurements. These distal peaks should be described by Equation 5 with the same R_0 value as the proximal peaks, but with different values of d_0 and θ , reflecting the differences in the geometric relationships between the proximal H3 tail and the distal H3 tail to the Cy5-labeled DNA end. We therefore used a weighted, global fitting routine (using MATLAB's *lsqnonlin* function) to fit 5 parameters (R_0 , and a d_0 and a θ for the distal and proximal peaks) to our calibration data. Errors were obtained by a bootstrapping routine: the set of FRET values for each calibration construct was resampled with replacement 1000 times, and for each of these new sets of FRET values, a new Gaussian mixture model was fit to obtain 1000 new peak values and errors. Each set of bootstrapped values were then fit to Equation 5, and the standard deviations of the fit parameters from bootstrapped samples taken to be the errors on the fit parameters.

The result of this fit is shown in [Data S4C](#) (solid curves), and the fit parameters are given in [Data S6](#). We note that $d_{\perp, \text{dist}} \approx 8$ nm in the crystal structure, in good agreement with our fit value here (note that θ_{dist} is within error of 90° , and thus $d_{\perp, \text{dist}} \cong d_{0, \text{dist}}$). Moreover, if $d_{\perp, \text{prox}} = d_{0, \text{prox}} \sin(180^\circ - \theta_{\text{prox}})$, then $d_{\perp, \text{prox}} = 2.6$ nm, again in excellent agreement with our estimate based on the crystal structure. However, R_0 is about a factor of 2 larger than we would expect for Cy3-Cy5. Therefore we considered several modifications to [Equation 5](#).

Because it is difficult to measure 0 FRET precisely, we introduce the possibility of a vertical offset, FRET_0 , to obtain

$$\text{FRET}(n) = \frac{1}{1 + \frac{(d_0^2 + 0.1156n^2 - 0.68d_0n \cos \theta)^3}{R_0^6}} + \text{FRET}_0. \quad (\text{Equation 8})$$

Note that this expression requires a 7-parameter fit (R_0 , and a d_0 , θ , and FRET_0 for the distal and proximal peaks) to 14 data points. We can reduce the dimensionality again to 5 by assuming that $\theta_{\text{prox}} \approx \theta_{\text{dist}} \cong 90^\circ$, not unreasonable given the geometry suggested by the crystal structure. Then we would fit

$$\text{FRET}(n) = \frac{1}{1 + \frac{(d_0^2 + 0.1156n^2)^3}{R_0^6}} + \text{FRET}_0 \quad (\text{Equation 9})$$

to the 14 data points. The results of fitting these two modified expressions to our calibration data are shown in [Data S4C](#) (dashed and dotted curves), and the fit parameters given in [Data S6](#).

These three equations for $\text{FRET}(n)$ ([Equations 5](#), [8](#), and [9](#)) differ very little in their ability to model the behavior of the proximal peaks, but none of them describe the distal peaks as well as they do the proximal peaks. Given that our goal here is to interpolate between our calibration data for the proximal peaks so that we can convert the FRET states explored during remodeling to base-pairs of DNA translocated, all three equations accomplish this goal equally well. We prefer [Equation 5](#), primarily because in all fits that include a FRET_0 parameter, the fitted values are, with one exception, within error of zero. Therefore we do not see a need to include FRET_0 , since the fits are consistent with $\text{FRET}_0 = 0$. As noted above, the fit parameters for [Equation 5](#) are all reasonable, except for R_0 , which is a factor of 2 larger than we would expect. However, our data are clearly consistent with an R_0 closer to the expected value of 6 nm, depending on the assumptions made (as evidenced by the fits to [Equations 8](#) and [9](#)). Moreover, the derivation described here represents only a simplified approximation, neglecting, for example, any contributions of the flexibility of the histone tails, or their likely interactions with flanking DNA, especially as n gets larger. Importantly, the decision to use [Equation 5](#), [Equation 8](#), or [Equation 9](#) does not affect our results (for example, cdfs of step sizes as in [Figures S3D](#) and [S3E](#)).

We therefore use [Equation 5](#), with parameters $R_0 = 10.9$ nm, $d_0 = 5.8$ nm, and $\theta = 153.8^\circ$, in the rest of this work. To convert FRET values to base-pairs of DNA translocated out of the nucleosome, we invert [Equation 5](#) to obtain

$$n(\text{FRET}) = 0.34^{-1} \left(d_0 \cos \theta + \sqrt{d_0^2 (\cos^2 \theta - 1) + R_0^2 \left(\frac{1}{\text{FRET}} - 1 \right)^{1/3}} \right). \quad (\text{Equation 10})$$

Classification of bi-directional movement in [Figure 3](#)

We observe three kinds of behavior with the centered 78/78 constructs in [Figure 3](#): “unidirectional” remodeling, in which the nucleosome is moved out of FRET range and does not come back into FRET range before one of the dyes photobleaches (Class I); bidirectional movement, in which the nucleosome initially moves out of FRET range but then returns, and can persist in mid to high FRET even for very long durations, as in the right panel (Class II); and multi-directional movement, in which the nucleosome is continuously moved in and out of FRET range before photobleaching occurs (Class III). All of these traces were acquired under chase conditions, in that, as in [Figure 2](#), unbound INO80 is washed out as ATP is washed in. Double chase experiments are indicated by two vertical yellow lines, where an additional wash with either buffer or ATP was performed subsequent to the wash that added ATP to start the reaction (and concurrently washed out unbound INO80).

QUANTIFICATION AND STATISTICAL ANALYSIS

Error estimation for ensemble measurements

All ensemble measurements of rate constants are reported as the mean of three or more experimental replicates ($n = 3$), along with standard error of the mean (SEM). Significance was determined using unpaired, two-tailed t tests (shown as asterisks in some bar graphs). These values are reported in the figure legends. None of the data were excluded. Graphing and statistical analyses were done using GraphPad Prism 5.

Hidden Markov model (HMM) analysis for extracting pause durations and FRET values from smFRET data

As has become standard in the field, with the exception of the translocation rates in [Figure S3H](#), we quantified our smFRET data using a hidden Markov model (HMM) approach; that is, remodeling data were approximated as step functions, with the pause phases

modeled as states with Gaussian emissions, and the translocation phases as instantaneous transitions between pauses. However, long smFRET trajectories, like those observed for INO80, are subject to an increased number of artifacts, such as dye blinking or slight fluctuations in the noise, which can complicate quantification of smFRET trajectories. Rather than using an HMM software package specifically designed for smFRET (e.g., the vbFRET package; Bronson et al., 2009), in order to reduce the likelihood of the HMM identifying artifacts as real transitions, and to reduce analysis time, we adapted a computationally fast, versatile, open-source, python-based HMM library called pyhsmm (<https://github.com/mattij/pyhsmm>). The HMM code fits a discrete state HMM to each trajectory generated by Traces, operating on the raw (unsmoothed) acceptor and donor intensity signals.

We fit the models using Gibbs sampling. The posterior distributions on states were very concentrated, so we used a single sample from the end of each Gibbs sampling chain as an estimate of the hidden state sequence. We used a hierarchical Dirichlet process (HDP) prior to automatically select the number of states (pause phases) in each trace. Further, we made use of the “sticky” regularizer available in the pyhsmm library to penalize short-lived states and hence prevent the model from assigning new states to spurious noise events. We developed a combination of MATLAB and python code to run pyhsmm by shelling out of MATLAB’s IDE; this code is included in the Traces GitHub repository (<https://github.com/stephij/Traces>).

As shown in Figure S3A, we observe two predominant clusters of FRET values, at 0.57 and 0.95 FRET, in the absence of remodeler. These FRET states correspond to two of the four populations of nucleosomes that result from mixing unlabeled H3 with Cy3-labeled H3 during octamer formation: some nucleosomes will have a Cy3 label on the H3 proximal to the Cy5-labeled DNA end, resulting in the higher FRET state, and some will have a Cy3 label on the H3 distal to the Cy5-labeled DNA end, resulting in the mid-FRET state. There will also be a population of nucleosomes with both H3 histones unlabeled, which show no FRET; and a population with both copies of H3 labeled, which are distinguishable by two-step photobleaching of the Cy3 dye, and are excluded. We also excluded any trajectories to which pyhsmm fit an initial FRET value lower than 0.775 FRET, since nucleosomes with distally labeled H3’s do not provide as great a dynamic range for monitoring nucleosome remodeling. Each dataset (e.g., INO80 with 3/78 nucleosomes and saturating ATP) consists of about 100 trajectories collated from at least 5 different experiments. Errors are derived from a bootstrapping procedure performed over trajectories: for each dataset, the ≥ 100 trajectories were resampled with replacement, and reported values, such as the means of each pause duration, were recalculated for each bootstrapped sample. Reported errors are standard deviations of the bootstrapped values.

Quantification of translocation rates observed by smFRET

The HMM analysis we use to quantify pause durations is based on a common assumption in the field, that states are well-described as having Gaussian-distributed emissions and are separated by instantaneous transitions. This analysis, particularly using pyhsmm, has the advantage of being computationally fast, and accurate for modeling the pauses we observe. However, the translocation phases that separate the pauses are not instantaneous transitions, and so cannot be quantified by this approach.

We therefore developed a continuous-time Bayesian model for analyzing FRET data with non-instantaneous but still fast transitions. Our analysis tool, called Slopey (available at <https://github.com/stephij/slopey>), pairs a continuous-time prior with an explicit model of the camera used to acquire discrete-time images, enabling sub-frame inference over translocation durations. Posterior inference in the model is performed using a Metropolis-Hastings Markov chain Monte Carlo (MCMC) algorithm. A schematic of the Slopey algorithm is shown in Data S3.

The continuous-time prior is on the red- and green-channel intensity processes, which we model as non-Markovian continuous-time jump processes. We parameterize this jump process prior in terms of four distributions: (1) a distribution on intensities of the red channel in pause phases, from which red intensity values are sampled independently, (2) a distribution on pause duration times, from which pause durations are sampled independently, (3) a distribution on translocation times, from which translocation times are sampled independently, and (4) a distribution on affine transformations to produce a corresponding green-channel process from the red-channel process. In symbols, we denote the continuous-time red-channel intensity as $V_R(t)$ for $t \geq 0$ (Data S3A). A sample path of $V_R(t)$ is piecewise linear in time, and is constructed by first sampling a sequence of durations $\{d_k\}_{k=1}^{2K+1}$, where K is the number of translocation phases, independently according to

$$d_k \sim \begin{cases} \text{Gamma}(a, b), & k \text{ odd} \\ \text{Uniform}(c, d), & k \text{ even} \end{cases}$$

and setting a corresponding sequence of times according to $t_k = \sum_{k'=1}^k d_{k'}$ for $k = 1, 2, \dots, 2K + 1$ (e.g., the t_1 through t_4 in Data S3A). Note that odd indices k correspond to pause phases while even indices k correspond to translocation phases. We then sample a sequence of red-channel pause-phase intensities $\{V_R^k\}_{k \text{ odd}}$ independently according to

$$V_R^k \sim \text{Gamma}(e, f).$$

With these values we can write the red-channel intensity process as

$$V_R(t) = \begin{cases} (t_{k+1} - t)V_R^k + (t - t_k)V_R^{k+1}, & t_k \leq t \leq t_{k+1}, k \text{ even} \\ V_R^k, & t_k \leq t \leq t_{k+1}, k \text{ odd} \end{cases}$$

for $k = 0, 2, \dots, 2K$, taking $t_0 = 0$. Finally, we write the green-channel intensity process as

$$V_G(t) = \alpha(\max_k V_R^k - V_R(t)) + \beta,$$

where $\alpha \sim \text{Gamma}(g, h)$ and $\beta \sim \text{Gamma}(i, j)$ independently.

We use a uniform prior on the translocation phase durations, with prior hyperparameters of minimum duration $c = 0.14$ seconds (1 frame) and maximum duration $d = 4.5$ seconds. We use an exponential prior on pause durations, with a prior hyperparameter of average duration 50 s (taking $a = 1$ and $b = 1/50$). The prior hyperparameters for red-channel (acceptor) intensities are $e = 1$, $f = 2.5$. The prior hyperparameters for the affine transformation from red-channel intensities to green-channel intensities are hyperparameters $g = 3$, $h = 3$, $i = 1$, $j = 5$.

These continuous-time red- and green-channel intensity processes are measured by the camera, which produces a discrete-time sequence of red- and green-channel frames with additive Gaussian noise (Data S3B). For each frame and each channel, the measured value is computed by integrating over a shutter period determined by the camera parameters T_{cycle} and T_{blank} (Data S3C). A random phase of $u \sim \text{Uniform}(0, T_{\text{cycle}})$ is included (Data S3B). Finally, additive Gaussian noise is added with standard deviation $\sigma = 0.075$ (Data S3D).

We initialized the Metropolis-Hastings MCMC trajectories using the HMM fit from pyhsmm, and ran each Markov chain for 10^5 iterations, collecting 200 evenly spaced iterates from the second half of each trajectory to form Monte Carlo estimates of pause and translocation durations. For each estimate we report standard errors (not posterior standard deviations) obtained via a bootstrapping procedure over trajectories (as with the pyhsmm algorithm described above).

Translocation by INO80 is fast, even at 0.1 mM ATP, making it difficult to identify with confidence the times at which translocation phases begin and end when the distance translocated is short (less than ~ 5 bp). Therefore for each trajectory, we measured the duration of the longest translocation, and averaged these durations to obtain the mean values reported in Figure S3H. In most cases, the translocation duration included in the reported average was the first translocation, except in those cases where distance translocated between p_{initial} and p_{second} was short (again, less than ~ 5 bp).

DATA AND SOFTWARE AVAILABILITY

Traces: Software for obtaining intensity-versus-time information from microscope images, available at <https://github.com/stephij/Traces>. Includes code for extracting pause durations using the pyhsmm HMM package.

Slopey: Software for quantifying non-instantaneous transitions between states with Gaussian emissions in smFRET data, available at <https://github.com/stephij>.

Molecular Cell, Volume 69

Supplemental Information

**The Yeast INO80 Complex Operates
as a Tunable DNA Length-Sensitive Switch
to Regulate Nucleosome Sliding**

Coral Y. Zhou, Stephanie L. Johnson, Laura J. Lee, Adam D. Longhurst, Sean L. Beckwith, Matthew J. Johnson, Ashby J. Morrison, and Geeta J. Narlikar

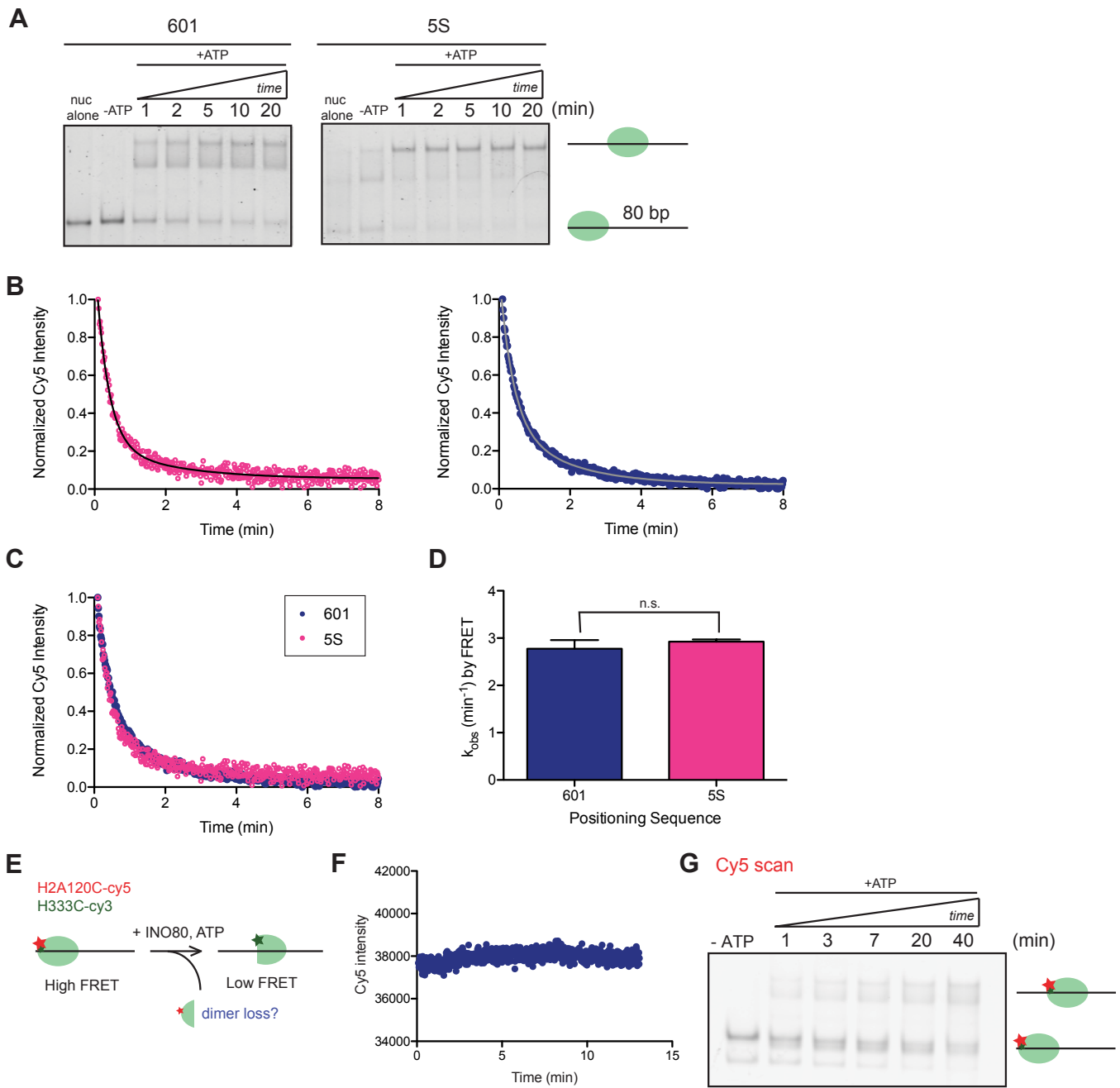


Figure S1, related to Figure 1.

(A) Native gel of remodeling timecourse with 0/80 nucleosomes positioned with either the 601 sequence (blue) or the naturally occurring 5S sequence (pink), which is 100-fold weaker at positioning nucleosomes (Partensky and Narlikar, 2009), and which also contains a different 80 bp flanking sequence outside of the positioning sequence. We hypothesized that the distribution of products observed with 601 0/80 nucleosomes (namely, the doublet product band) could represent sequence-specific variations in the strength of the histone-DNA contacts near the center position of the 0/80 construct's DNA. Consistent with this hypothesis, we find that with 0/80 nucleosomes positioned by 5S, the final distribution of products by native gel becomes more similar to that of the 0/60 nucleosomes positioned by 601 (Figure 1A), with a discrete centered product band.

(B)-(C) Raw data showing ensemble FRET remodeling of 601- or 5S-positioned 0/80 nucleosomes, separately (B) or overlaid for direct visual comparison (C). Solid curves in B are fits to Equation 2 (see Methods).

(D) Quantification of the rate constants of FRET remodeling for either 601 or 5S 0/80 nucleosomes. These experiments were performed under single turnover conditions and with saturating enzyme and ATP. The overall remodeling rate constant is the same for 601 and 5S nucleosomes, indicating that sequence affects final product distribution but not remodeling rate constants. Data represent the mean \pm S.E.M for three replicates.

(E) Some previous studies have suggested that under certain conditions, yeast INO80 exhibits H2A/H2B dimer exchange activity (Brahma et al., 2017; Papamichos-Chronakis et al., 2011; Watanabe et al., 2013), raising the possibility that dimer loss may play a role in nucleosome sliding. To test for this possibility, we engineered a FRET pair between the histones H2A and H3 that would report on dimer loss. H2A is labeled with Cy5 and H3 with Cy3 such that the two fluorescent dyes start in close proximity, and therefore in high FRET. Loss of dimers from the nucleosome would remove the Cy5 acceptor, leading to a loss of Cy5 intensity in both panels (F) and (G). Nucleosomes here have 80 bp flanking DNA.

(F) Example recording of ensemble Cy5 intensity over time. Here Cy3 is directly excited, so a stable Cy5 intensity indicates no change in distance between the dyes (and therefore no change in the FRET excitation of Cy5), over \sim 12 minutes. We did not observe any decrease in FRET over the same period of time that sliding occurs, suggesting that H2A/H2B dimer loss is not essential for nucleosome sliding.

(G) Native gel showing remodeling of the nucleosomes in E, demonstrating that sliding is occurring on timescales comparable to those shown in F.

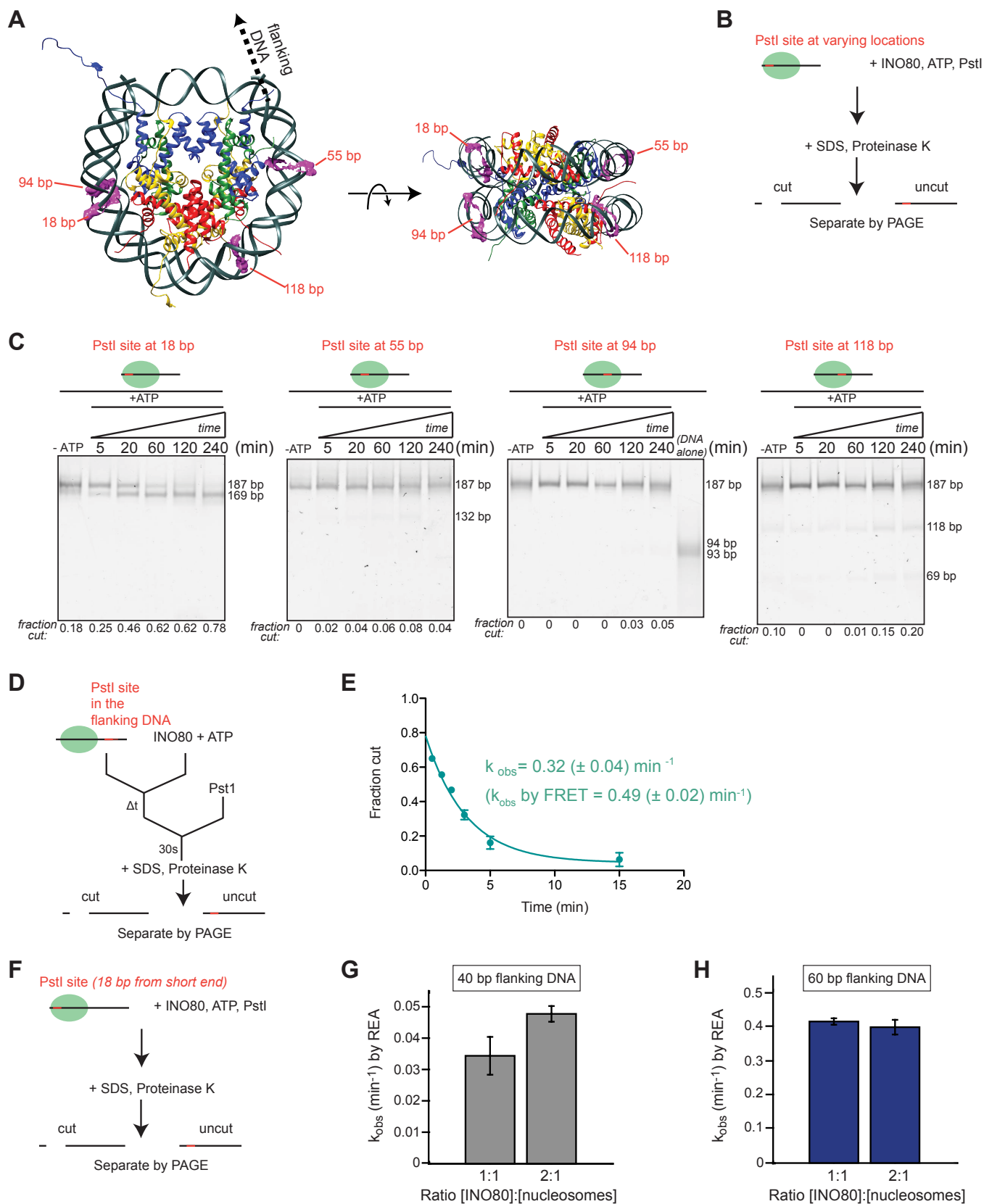


Figure S2, related to Figure 1.

(A) Crystal structure of the nucleosome (PDBID 1AOI (Luger et al., 1997)) with locations of engineered PstI restriction sites indicated.

(B) Design of the REA assay when the PstI site is varied within the nucleosome core.

(C) PAGE separation of cut and uncut DNA fragments from the REA assay schematized in B. The fraction cut is quantified below each lane. In the case of the PstI site at 94, so little cutting was observed that the DNA alone was cut and run as a size standard. INO80's ability to generate an intermediate with altered DNA accessibility is reminiscent of "remosomes" and other nucleosome structures with altered accessibility that have been described for SWI/SNF family remodelers (Lorch et al., 1998; Narlikar et al., 2001; Schnitzler et al., 1998; Shukla et al., 2010). Intriguingly, though, despite testing several positions for restriction enzyme accessibility, we only observe substantial cutting with the site 18 bp into the nucleosome, suggesting that the process described by k_{conf} (Figure 5) results in a localized change in histone-DNA contacts. SWI/SNF remodelers, on the other hand, generate structures with altered restriction enzyme accessibility throughout the nucleosome (Fan et al., 2003; Narlikar et al., 2001). While it could be the case that bound INO80 precludes detection of conformational changes at other locations in the nucleosome, another interpretation is that INO80 unpeels the DNA near the exit site, which may specifically loosen contacts between the H2A/H2B dimer and DNA. This interpretation is consistent with recently published work suggesting that unlike other remodeling enzymes, INO80 translocates near the H2A/H2B dimer (Brahma et al., 2017).

(D) Design of an REA assay to measure occlusion of a PstI site initially located in the flanking DNA, rather than the nucleosome core, to control for any intrinsic differences in the FRET and REA assays arising from possible technical artifacts. Occlusion of this site as measured by REA is expected to report on nucleosome sliding, similarly to remodeling by FRET. Flanking DNA here is 60 bp; the PstI site is 10 bp from the right edge of the nucleosome in its initial position.

(E) Quantification of the fraction of DNA cut over time with the PstI site in the flanking DNA. Rate constant obtained from the fit (see Methods) is shown above the data, along with the rate constant for the overall remodeling rate measured by FRET. For this experiment, 100 μM ATP was used instead of 1 mM. Rate constants are mean \pm S.E.M. The rate of occlusion of the external restriction site is comparable to the rate of remodeling by ensemble FRET, ruling out artifactual differences between the two assays.

(F) Our REA results are not affected by a change in the stoichiometry of INO80 on 0/40 versus 0/60 nucleosomes as measured by remodeling activity. This schematic of the REA accessibility assay used for titration experiments is the same as Figure 1E.

(G) Quantification of the rate constants for cutting by Pst1 for 0/40 nucleosomes, with two different ratios of INO80 concentration to nucleosome concentration.

(H) Quantification of the rate constants for cutting by Pst1 for 0/60 nucleosomes, again with two different ratios of INO80 concentration to nucleosome concentration. The activity of INO80 on both 0/40 and 0/60 nucleosomes does not change significantly between an INO80:nucleosome ratio of 1:1 versus 2:1. These titrations cannot, however, definitively determine the absolute stoichiometry of yeast INO80 on these nucleosomes, because different methods were used to determine INO80 concentration and nucleosome concentrations. Data represent the means \pm S.E.M. for three replicates. These assays were performed under single turnover conditions and with saturating enzyme and ATP.

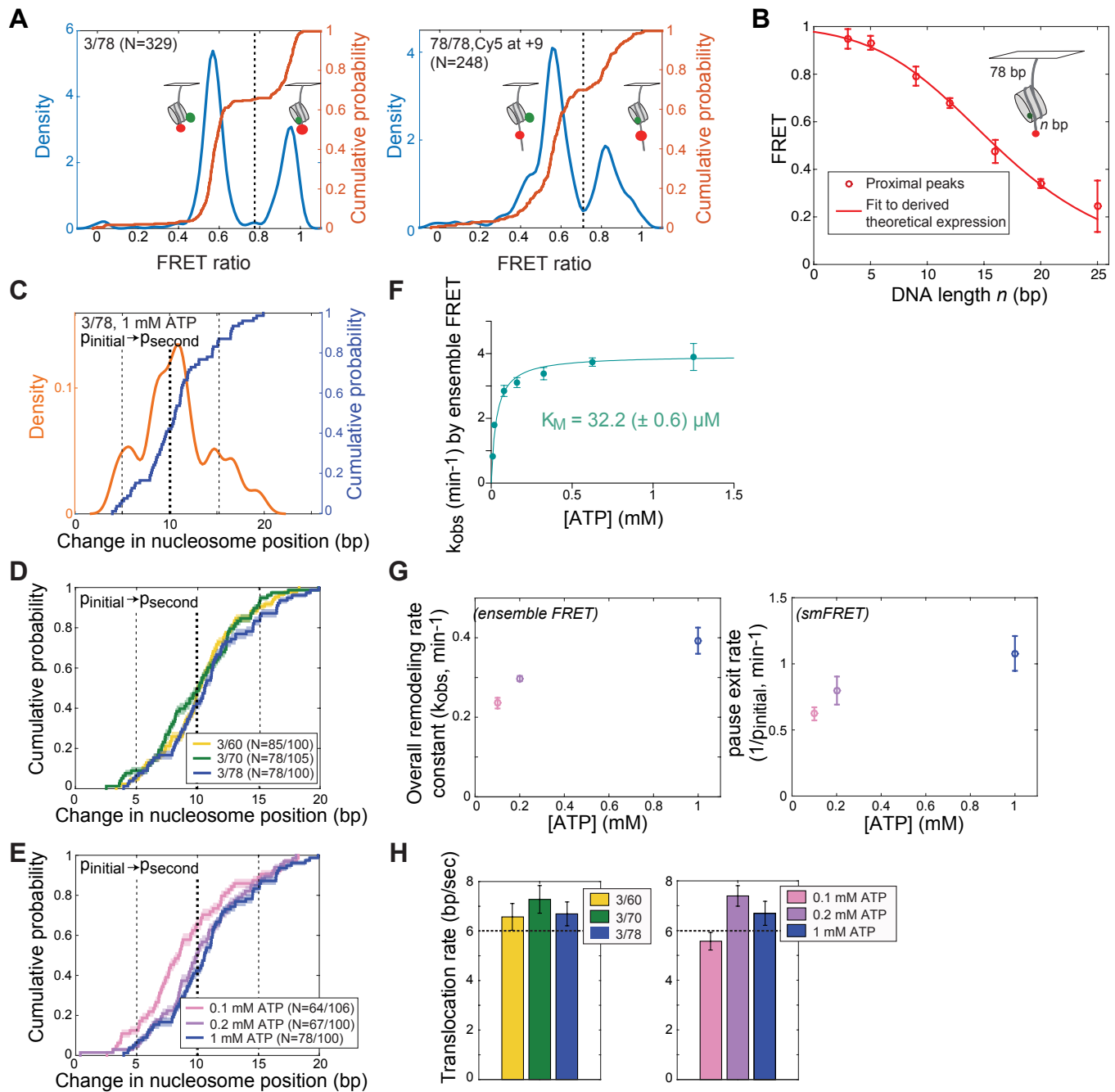


Figure S3, related to Figure 2.

(A) Kernel density estimation plots (KDEs, blue) and empirical cumulative probabilities (CDFs, orange) of initial FRET values for 3/78 nucleosomes with the Cy5 on the DNA end (left), and 78/78 nucleosomes with the Cy5 at 9 bp from the edge of 601 (right). KDEs are conceptually similar to histograms, but are smoothed rather than binned, which reduces the potential for generating artificial clusters or “peaks” in the data based on choice of bin width and location. The two peaks in the KDE plots correspond to two expected populations of nucleosomes: one population in which the H3 proximal to the Cy5-labeled DNA end is Cy3 labeled, resulting in higher initial FRET, and one in which the distal H3 has the Cy3 label. All data in this work (including with the 5S nucleosomes in Supplemental Figure S4) were collected from nucleosomes in the proximally labeled H3 population. Nucleosomes with neither H3 labeled are invisible; those with both H3’s labeled with Cy3 exhibit two-step photobleaching in the Cy3 channel and are excluded from these histograms as well as from remodeling datasets. The CDFs represent the same information as the KDEs but without the smoothing filter; peaks in the KDEs appear in the CDFs as steep slopes. Nucleosomes here are in the presence of 1 mM ATP but in the absence of remodeler. N indicates the number of nucleosomes included in the KDE and CDF; vertical black dashed lines indicate the lower threshold FRET value for nucleosomes to be classified as starting with a proximal H3 label and thus included for further analysis. KDE bandwidths are 0.025. Data for 3/78 are the same as in Data File S4A.

(B) Calibration curve showing the average FRET value of the proximal Cy3 dye as a function of bp of flanking DNA, n . This calibration curve allows us to convert FRET values measured during remodeling to bp DNA moved out of the nucleosome. Red curve is a fit to our derived theoretical expression for FRET as a function of n (see Methods and Data File S4). Errors on the data are standard deviations from fits of Gaussian mixture models to CDFs of FRET values for each construct (see Data File S4).

(C) An example combined KDE and CDF plot for the distance the nucleosome is moved in the first translocation phase (that is, the distance the nucleosome is moved between p_{initial} and p_{second}). The major peak in the KDE corresponds to the steepest slope in the CDF, and indicates that most nucleosomes are moved about 10 bp between p_{initial} and p_{second} (alternatively, note that the cumulative probability is roughly 0.5 at 10 bp, indicating that half the nucleosomes are moved 10 bp or fewer during the first translocation event). Although KDEs are more intuitive, being conceptually similar to histograms, they are less preferable for making quantitative comparisons, because peaks can “appear” or “disappear” in the data as the smoothing parameter is varied. Therefore in D and E, we show only CDFs in order to make comparisons between data sets. The KDE here has a Gaussian kernel with bandwidth 0.025.

(D) CDFs showing the distance a nucleosome is moved between p_{initial} and p_{second} , as a function of flanking DNA length. The steepest slope occurs for all three constructs primarily at 10 bp of movement, and secondarily at 5 or 15 bp. An alternative summary of the information in these CDFs is that roughly half of the nucleosomes are moved 10 bp or fewer during the first translocation event; but only about 5%-10% of them move fewer than 7-8 bp, and $\sim 80\%$ move 12 bp or fewer. This again indicates that 8-12 bp is the predominant distance the nucleosomes is moved between the initial and secondary pauses, for the traces that have a secondary pause within FRET range. N in the legend indicates how many traces were included in these plots; only traces with distinct secondary pauses within FRET range (about 75% of the data) were included. Errors are indicated as shaded areas around the solid curves and are obtained via a bootstrapping procedure (see Methods).

(E) Same as D but as a function of ATP concentration. It appears that at 0.1 mM ATP, the step size (that is, the number of bp the nucleosome is moved between p_{initial} and p_{second}) decreases. This could suggest that at low ATP concentrations, INO80 may get “stuck” at more locations as the DNA is moved over the histone octamer, rather than pausing only at the locations of the most favorable DNA-histone contacts.

(F) Rate constants of 0/80 nucleosomes as measured by ensemble FRET, at 30°C, with saturating INO80

and varying concentrations of ATP. The ATP concentrations tested by smFRET (Figure 2E, this figure) are all well above the K_m of $32.2 \mu\text{M}$, but below 0.1 mM ATP, remodeling becomes too slow relative to the photobleaching rate, and so lower concentrations are technically infeasible to measure. Data represent means \pm S.E.M. for three replicates.

(G) Left, overall ensemble FRET remodeling rate as a function of ATP concentration for 3/78 nucleosomes. In contrast to the experiments in F, and for better comparison with the smFRET experiments, these experiments were performed at 20°C (but still under single turnover conditions, with saturating enzyme and ATP). Data represent means \pm S.E.M. for three replicates. Right, the inverse of the p_{initial} durations in Figure 2E, as a function of ATP concentration. Most, if not all, of the observed reduction in overall remodeling rate measured by ensemble FRET can be attributed to an increase in the duration of p_{initial} (i.e., a decrease in $1/p_{\text{initial}}$).

(H) Rate of nucleosome sliding as a function of flanking DNA length (left) or ATP concentration (right). The small but statistically significant decrease in translocation rate below 0.2 mM ATP (indicated by dashed line) is comparable to the effect of ATP on the translocation rate of ACF in a similar concentration range (Blosser et al., 2009). Data represent means \pm S.E.M. obtained via a bootstrapping procedure (see Methods).

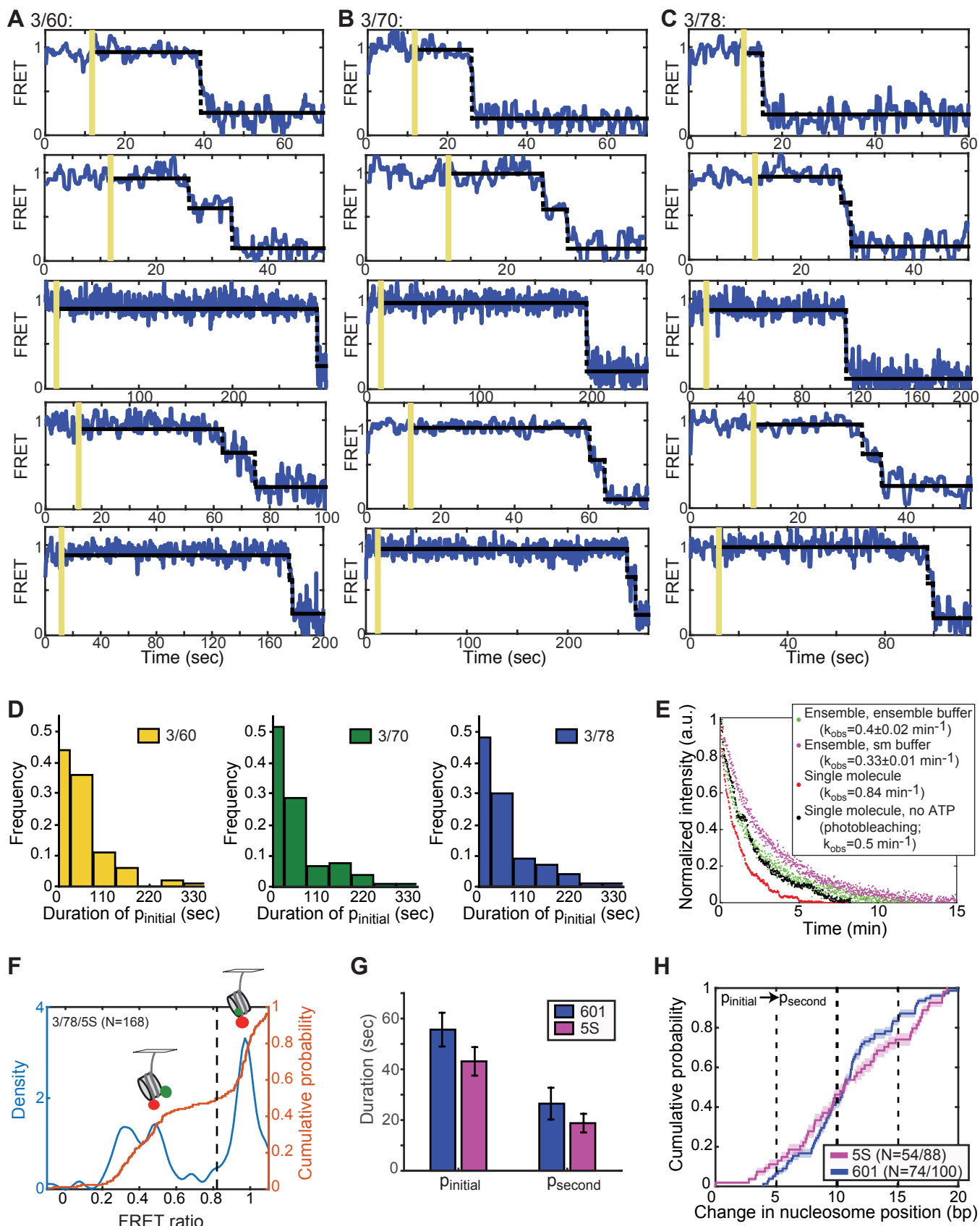


Figure S4, related to Figure 2.

(A) Example timecourses of remodeling of 3/60 nucleosomes in the presence of 1 mM ATP, plotted as in Figure 2B. Black line is the segmentation of the data obtained by the discrete state HMM (pyhsmm; see Methods), showing pauses identified. Note that the x-axis scales vary widely between plots.

(B) Example timecourses of remodeling of 3/70 nucleosomes in the presence of 1 mM ATP.

(C) Example timecourses of remodeling of 3/78 nucleosomes in the presence of 1 mM ATP (see also Figure 2B).

(D) Histograms of p_{initial} durations for 3/60, 3/70, and 3/78 nucleosomes in the presence of 1 mM ATP. To first order approximation, these durations are exponentially distributed.

(E) Comparison between ensemble FRET remodeling rates in ensemble buffer versus the imaging buffer used for smFRET, and between these rates and sliding rates observed by smFRET. Data are with 3/78 nucleosomes, saturating ATP (1 mM) and saturating enzyme (15 nM), at 20°C and under single turnover conditions. Ensemble FRET rate constants are means and S.E.M. from three replicates. smFRET data were converted to “pseudo-ensemble” data by summing the intensities of all Cy5 molecules included in the smFRET dataset, and then binning into 1-second intervals as in our ensemble FRET data. Note that this “pseudo-ensemble” data reports in changes in FRET only for events that are clearly sliding: events that look like photobleaching (an instantaneous transition from high FRET to zero FRET within one frame) were excluded. The black data, on the other hand, represent pseudo-ensemble smFRET data in the absence of ATP, in which all quantified events were photobleaching events. We note that ensemble FRET remodeling (green and purple) is slower than the sliding rates observed by smFRET (red), suggesting that attachment of the nucleosome to the surface of the microscope slide does not adversely impact remodeling (which is also the case for other remodelers, including large complexes like RSC (Blosser et al., 2009; Harada et al., 2016)). We note also that because of the way these experiments are performed, the smFRET data are under chase conditions, while the ensemble FRET data are not. Further discussion of the differences between the ensemble FRET and pseudo-ensemble smFRET data can be found in the Results and Discussion sections of the main text.

(F) To test the hypothesis that the secondary pauses observed by smFRET are a consequence of sequence-specific histone-DNA interactions, rather than reflecting part of INO80’s remodeling mechanism, we quantified the durations of p_{initial} and p_{second} and the locations at which p_{second} occurs with a 3/78 construct containing the 5S positioning sequence instead of the 601 sequence. Here we show a KDE and CDF of initial FRET values of 5S nucleosomes (see also Supplemental Figure S3). KDE bandwidth is 0.025.

(G) Initial and secondary pause durations with 3/78 nucleosomes containing either the 601 positioning sequence or the 5S positioning sequence. We observe similar overall remodeling rates with 5S and 601 by ensemble FRET (Supplemental Figure S1), which is consistent with the duration of p_{initial} , which dominates the reaction, being insensitive to sequence. (Although there appears to be a trend towards shorter pauses with 5S nucleosomes, this trend is not statistically significant.) Data represent means \pm S.E.M. obtained via a bootstrapping procedure (see Methods).

(H) CDFs of the step size as a function of positioning sequence (see also Supplemental Figure S3). The overall slope of the CDF is reduced for 5S compared to 601, indicating that with 5S nucleosomes, there is not as strong a preference for moving the nucleosome 10 bp. That is, roughly half of the nucleosomes are moved 10 bp or fewer in the first translocation event with both 601 and 5S nucleosomes; but more of them (\sim 10%) are moved 5 bp or fewer with 5S, compared to 601, in which only about 5% are moved 5 bp or fewer. Similarly, \sim 80% of the nucleosomes are moved 15 bp or fewer with 601, but only about 75% with 5S. This increased diversity in step size is consistent with the 5S sequence, as a weaker positioning sequence than 601, having a reduced preference for its rotational positioning on the octamer compared to 601 (Hall et al., 2009; Partensky and Narlikar, 2009). These results are in contrast to what has been observed with ACF, in which sequence does not affect the locations of the pauses (Blosser et al., 2009), and suggest that

INO80 might pause during translocation not as a regulatory aspect of its mechanism, but at sites where the DNA forms favorable contacts with the histone core (Hall et al., 2009). Such behavior would be similar to RNA Polymerase II pausing at points of strong DNA-histone interactions while translocating through a nucleosome (Bondarenko et al., 2006; Gaykalova et al., 2015), as well as with the results described above, in which a sequence-specific difference in product distribution is observed by native gel (Supplemental Figure S1A).

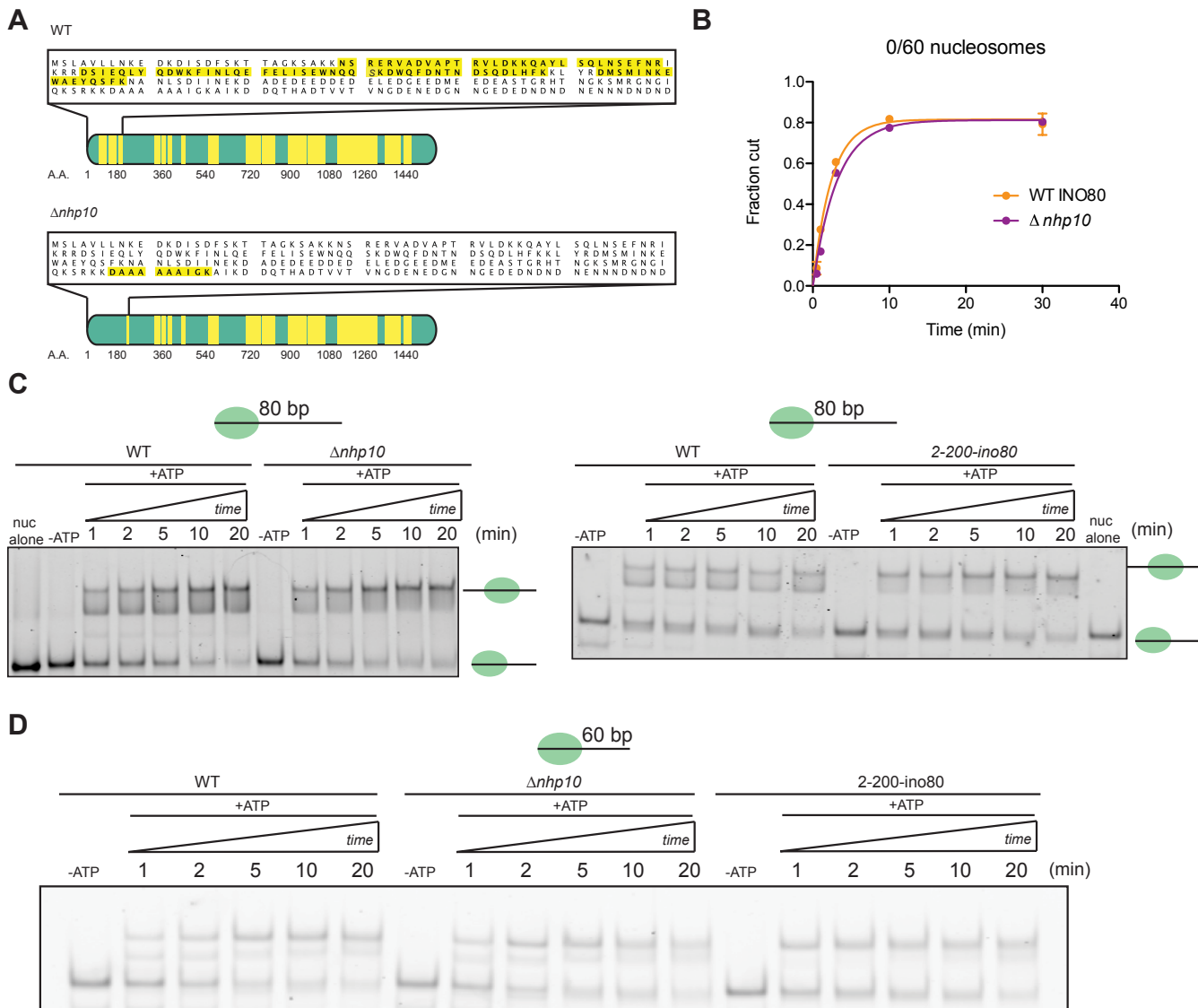


Figure S5, related to Figure 4. (A) Summary of mass spectrometry data of the Ino80 ATPase protein isolated from either WT (top) or $\Delta nhp10$ (bottom) yeast. The secondary structure of the Ino80 protein is shown in teal, with peptides identified indicated in yellow. The sequence of the N-terminus is shown as a box above each structure, with the identified peptide sequences highlighted in yellow. (B) Quantification of fraction cut by REA on 0/60 nucleosomes, with either INO80(WT) or INO80($\Delta nhp10$). See also Figure 4(D)-(F). (C) Native gel remodeling of 0/80 nucleosomes by WT INO80, INO80($\Delta nhp10$) and INO80($\Delta 2-200-ino80$). (D) Native gel remodeling of 0/60 nucleosomes by WT INO80, INO80($\Delta nhp10$) and INO80($\Delta 2-200-ino80$). Assays in (C) and (D) were performed under single turnover conditions and with saturating enzyme and ATP.

"0/100":
 5' - /5Cy3 / CTGGAGAATCCCGGTGCCGAGGCCGCTCAATTGGTCGTAGACAGCTCTAGCACCGCTTAAACGCACGTACGCGCTGTCCCCGCGTTTTAACCG...
 3' - GACCTCTTAGGGCCACGGCTCCGGCGAGTTAACACGATCTGTGAGATCGTGGCGAATTTGCGTGCATGCGCGACAGGGGGCGCAAATTTGGC...

...CCAAGGGGATTACTCCCTAGTCTCCAGGCACGTGTGATATATACATCCTGTGCATCTATTGAACAGCGACCTTGCCGGTGCCAGTCGGATAGTGTCCGAG...
...GGTTCCCCTAATGAGGGATCAGAGGTCCTGTCACAGTCTATATATGTAGGACACGTAGATAACTTGTGCTGGAACGGCCACGGTCAGCCTATCAGAAGGCTC...

...CTCCACTCTAGAGGATCCCGGGTACCGAGCTCGAATTCGCCCTATA-3'
...GAGGTGAGATCTCCTAGGGGCCATGGCTCGAGCTTAAGCGGGATAT-5'

"3/78":
 5' - /5Cy5 / GCCCTGGAGAATCCCGGTCTGCAGGCCGCTCAATTGGTCGTAGACAGCTCTAGCACCGCTTAAACGCACGTACGCGCTGTCCCCGCGTTTTAACCG...
 3' - CGGGACCTCTTAGGGCCAGCGTCCGGCGAGTTAACACGATCTGTGAGATCGTGGCGAATTTGCGTGCATGCGCGACAGGGGGCGCAAATTTGGC...

...CCAAGGGGATTACTCCCTAGTCTCCAGGCACGTGTGATATATACATCCTGTGCATCTATTGAACAGCGACCTTGCCGGTGCCAGTCGGATAGTGTCCGAG...
...GGTTCCCCTAATGAGGGATCAGAGGTCCTGTCACAGTCTATATATGTAGGACACGTAGATAACTTGTGCTGGAACGGCCACGGTCAGCCTATCAGAAGGCTC...

...CTCCACTCTAGAGGATCCCGGGTACC-3'
...GAGGTGAGATCTCCTAGGGGCCATGG/5Bioteg/-5'

"3/78/5S" and "0/80/5S":
 5' - /5Cy5 / CCAGGCCGACCTGCTGGCTGCAGAGATCAGACGATATCGGGCACTTTCAGGGTGGTATGGCCGTAGGCGAGCACAGGCTGACTTTTCCTCCCC...
 3' - GGTCCGGCTGGGACGAACC**GACGTC**CTAGTCTGCTATAGCCCGTGAAGTCCACCATACCGGGATCCGCTCGTGTCCGACTGAAAAGGAGGGG...

...TTGTGCTGCCTTCTGGGGGGGCCAGCCGGATCCCGGGCGAGCTCGAATTCGTAATCATGTCATAGCTGTTTCCTGTGAAATTTATCCGCTCACAAT...
...AACACGACGGAAGACCCCCCGGGTCGGCCTAGGGGCCGCTCGAGCTTAAGCATTAGTACAGTATCGACAAAGGACACACTTTAAACAATAGGCGAGTGTTA...

...TCCACACAACATACGAGCCGGAAGCATAA-3'
...AGGTGTGTTGATGCTCGGCCTTCGTATT/5Bioteg/-5'

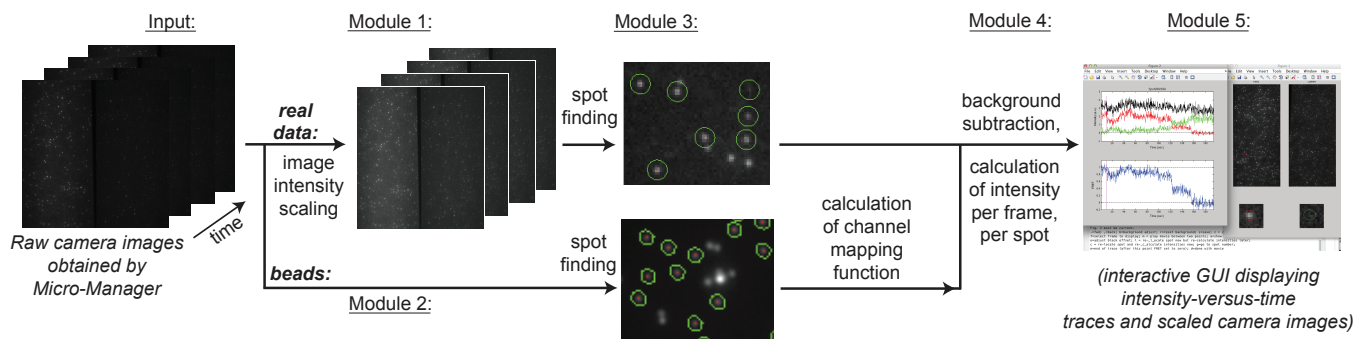
"78-78":
 5' - GGATCCTAATGACCAAGAAAGCATGATTCCTCACACCGAGTTTCATCCCTTATGTGATGGACCTATAC*T*CGGCCGCCCTGGAGAATCCCGGT**CTGCAGGC**...
 3' - CCTAGGATTACTGTTCCCTTCGTACTAAGAAAGTGTGGCTCAAGTAGGGAATACACTACCTGGGATATG C GCCGGCGG**GACCTCTTAGGGCCAGCGTCCG**...

...CGCTCAATTGGTCGTAGACAGCTCTAGCACCGCTTAAACGCACGTACGCGCTGTCCCCGCGTTTTAACCGCCAAGGGGATTACTCCCTAGTCTCCAGGCAGC...
...GCGAGTTAACAGCATCTGTGAGATCGTGGCGAATTTGCGTGCATGCGCGACAGGGGGCGCAAATTTGCGGTTCCCTAATGAGGGATCAGAGGTCCTGTC...

...TGTCAGATATATACATCCTGTGCATCTATTGAACAGCGACCTTGCCGGTGCCAGTCGGATAGTGTTCGAGCTCCACTCTAGAGGATCCCGGGT...
...ACAGTCTATATATGTAGGACACGTAGATAACTTGTGCTGGAACGGCCACGGTCAGCCTATCAGAAGGCTCGAGGGTGAGATCTCCTAGGGGCCA...

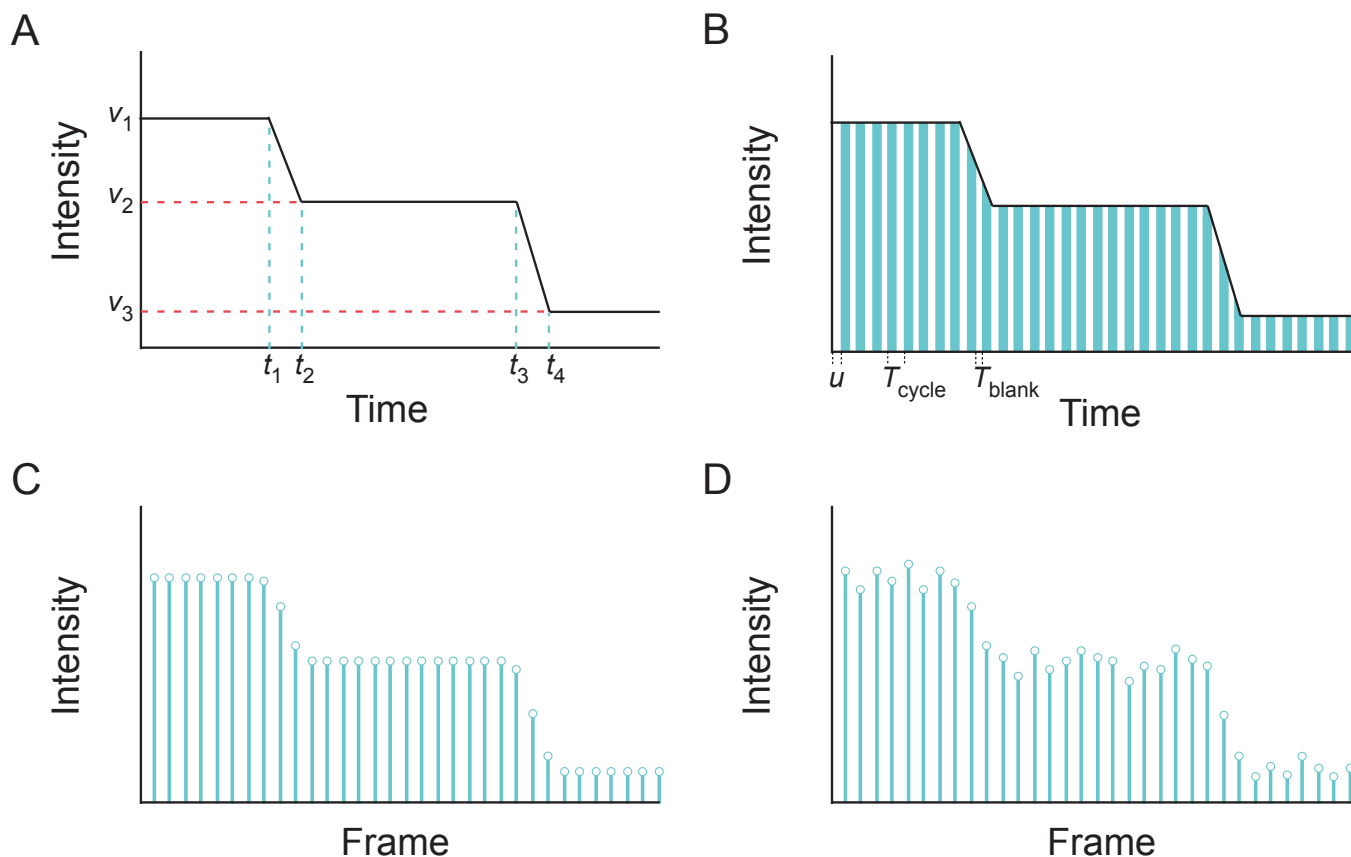
...ACC-3'
...TGG/5Bioteg/-5'

Data File S1, related to STAR Methods. Nucleosomal DNAs used in this work. The nucleosome positioning sequence (601 for all constructs except "3/78/5S" and "0/80/5S") is underlined; a Pst1 restriction enzyme recognition site, if present, is in boldface blue. The nucleotide in 78/78 to which the internal Cy5 is conjugated is flanked by asterisks. The two additional bases on the long end of 0/80/5S, compared to 3/78/5S, are highlighted in yellow. The 0/80/5S construct also has a Cy3 label instead of the Cy5 shown here, and no biotin on the other end. All other DNAs used in this work can be derived from these sequences (e.g. 0/40, 0/60, and 0/80 DNAs used for ensemble FRET are truncations of the 0/100 construct; the 3/60 and 3/70 constructs used for smFRET are truncations of 3/78; etc.) Constructs shown here are for FRET-labeled nucleosomes; REA constructs have the Cy3 on the 5' end of the opposite DNA strand (that is, on the long flanking DNA).

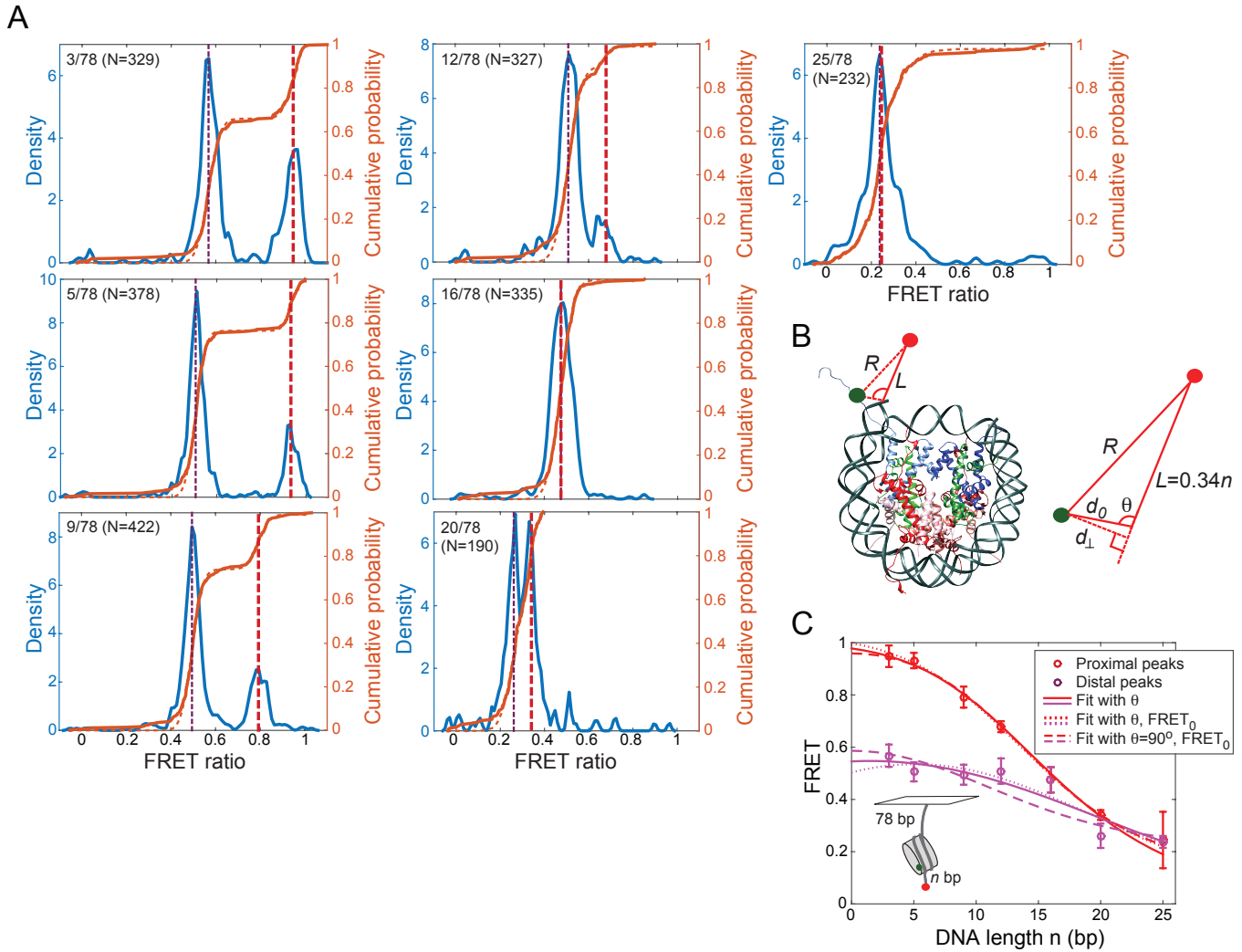


Data File S2, related to STAR Methods. Summary of the Traces smFRET analysis software.

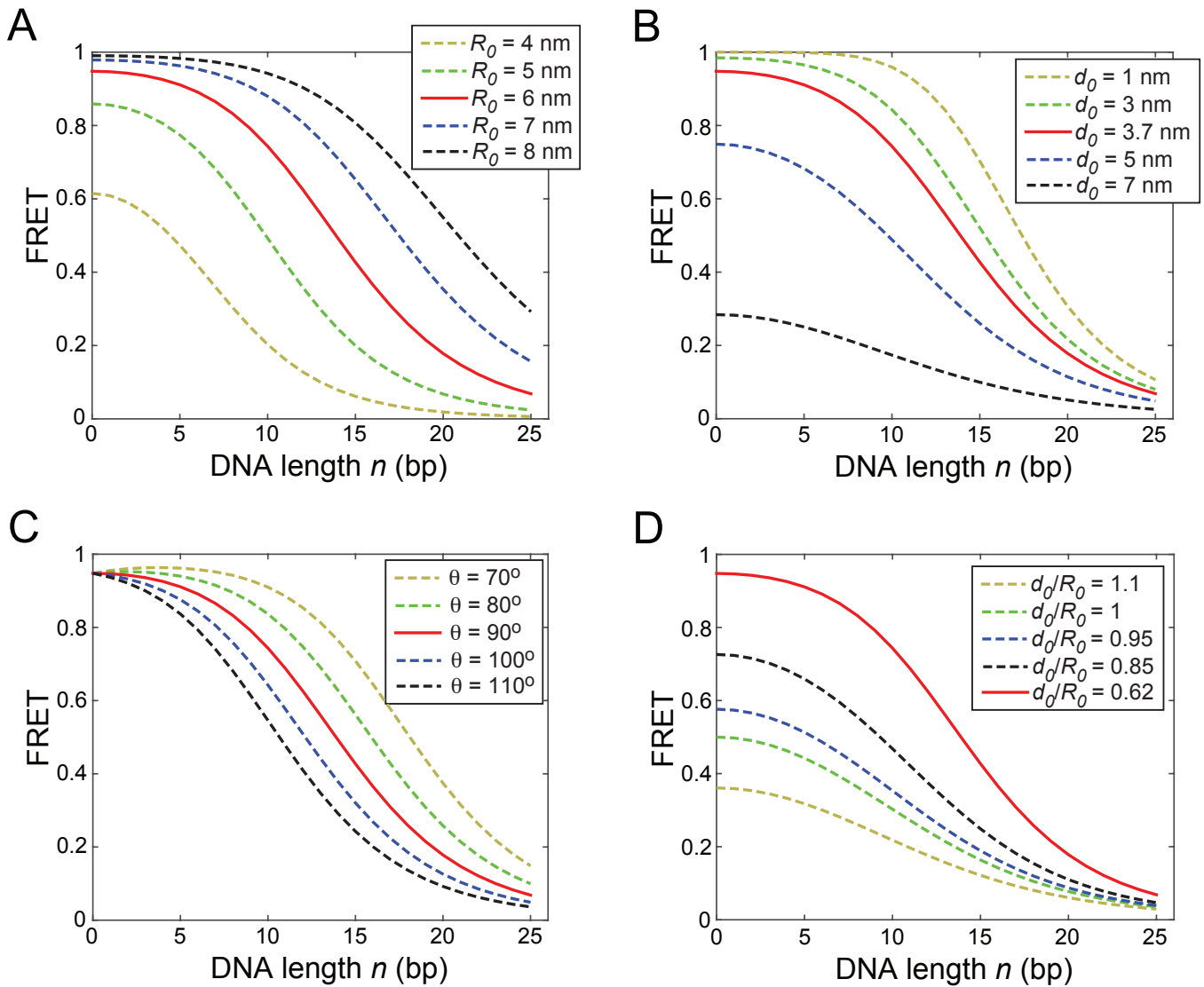
The workflow for analyzing smFRET data can be divided into 5 modules: (1) data pre-processing, which includes scaling each image to take advantage of the full dynamic range of the numeric type used; (2) finding a mapping between donor and acceptor channels, which will never be perfectly aligned in any setup, and which we accomplish by fitting a polynomial transformation to paired images of surface-attached, microscopic fluorescent beads; (3) spot finding, or identifying which pixels in each channel contain real fluorescence vs. background fluctuations; (4) calculation of the intensity of each identified spot in each frame of a movie; and (5) displaying these time trajectories (“traces”) for the user to pick out results for further analysis. The GUI that accomplishes Module 5 in Traces also provides options for the user to refine the localization of each spot (for example, if the bead-based polynomial transformation was inaccurate for part of the field of view), adjust the background to be subtracted, crop parts of the trace for downstream analysis, and inspect the camera images that generated each trace. Traces can be downloaded from <https://github.com/stephlj/Traces>.



Data File S3, related to STAR Methods. Schematic summary of the Slopey algorithm for quantifying translocation events. (A) Idealized trajectory of acceptor dye intensity over time. The pause phases have acceptor intensities of v_1 , v_2 , and v_3 ; transitions from pause phases to translocation phases occur at times t_1 and t_3 , while transitions from translocation phases to pauses occur at times t_2 and t_4 . (B) Schematic of the camera model. Blue bars represent the times during which the camera is recording fluorescence intensity. An image frame acquired by the camera, which has total duration T_{cycle} , consists of the blue bars (the exposure time), plus T_{blank} , during which the information is transferred off of the camera chip into memory. Light intensity is not recorded during T_{blank} . We collect data with frame transfer off, such that $T_{cycle} = 135.6$ seconds and $T_{blank} = 35.6$ seconds for 100 ms exposure. Note that translocation events can begin at any point during T_{cycle} , including during T_{blank} . The offset parameter u represents the time between the beginning of the data trajectory and the first frame recorded by the camera. (C) Idealized total intensities collected during each frame. The height of each bar represents the area in each blue box in B. Note that if a translocation event begins mid-frame, as at time t_3 , the total intensity collected during that time will be less than during the preceding frame, but not as much less as if the frame were fully within the translocation phase. (D) We add i.i.d. (independent and identically distributed) Gaussian noise with a variance of 0.075 to the idealized camera output in C to obtain our final model of acceptor intensity data. Given the data, the prior and this model of the data, Slopey infers u , $\{v_n\}$, and $\{t_n\}$ and the channel transform parameters a and b (see Methods). Slopey can be downloaded from <https://github.com/stephly/slopey>.



Data File S4, related to STAR Methods. Approach to microscope calibration. (A) We generated a series of nucleosomal constructs with varying lengths of DNA, n , between the Cy5 label and the nucleosome, and measured the resulting FRET for these constructs in the absence of remodeler. Nucleosomes are labeled as $n/78$, indicating n bp of DNA between the Cy5 and nucleosome edge, and 78 bp between the nucleosome and the surface. Each panel shows a KDE plot (blue), an empirical cdf (solid orange curve), and a fit of the cdf to a Gaussian mixture model (dashed orange curve) for determining peak locations and widths. N is the number of nucleosomes included in each data set. For $n \geq 16$ bp, the proximal and distal peaks exhibit overlapping FRET values, indicating that at these DNA lengths, the Cy3 labels on the two H3 tails are roughly equidistant in three dimensions to the Cy5 on the DNA end. 3/78 data are the same as in Supplemental Figure S3A. KDEs have Gaussian kernels with bandwidth 0.01. (B) Left, crystal structure of the nucleosome (PDBID 1AOI; (Luger et al., 1997)) illustrating the variables used to approximate the relationship between bp of DNA and inter-dye distance. Only the proximal H3 tail is shown with a Cy3 label. Right, a simplified diagram of our approximation of this geometric relationship. (C) Proximal and distal peak FRET values for the nucleosome series described in A, as a function of n . Solid curves represent a global fit of Equation 5 to the proximal and distal peaks; dashed curves, a fit to Equation 9; dotted curve, a fit to Equation 8. Errors on the data points are the standard deviations of the Gaussians obtained from the Gaussian mixture model fits. Solid curve is the same as in Supplemental Figure S3B.



Data File S5, related to STAR Methods. Behavior of our expression for FRET vs. flanking DNA length as a function of different parameters. Effects of the different parameters in Equation 5 on the shape of the FRET-vs- n curve. Solid red curve is the same in all panels and has parameters $R_0 = 6$ nm, $d_0 = 3.7$ nm, and $\theta = 90^\circ$.

Fit to:	R_0 (nm)	$d_{0,\text{prox}}$ (nm)	θ_{prox}	$\text{FRET}_{0,\text{prox}}$	$d_{0,\text{dist}}$ (nm)	θ_{dist}	$\text{FRET}_{0,\text{dist}}$
<i>(expected)</i>	6 (Murphy et al., 2004)	$\sim 2-4$	$> 90^\circ$		~ 8	$\sim 90^\circ$	
Eq. 5	10.9 ± 1.1	5.8 ± 1.0	$153.8 \pm 20.6^\circ$	-	10.6 ± 1.0	$87.3 \pm 12.0^\circ$	-
Eq. 8	8.3 ± 2.2	5.7 ± 0.7	$105.8 \pm 40.6^\circ$	0.09 ± 0.17	8.6 ± 1.8	$78.3 \pm 9.8^\circ$	0.06 ± 0.21
Eq. 9	6.7 ± 0.3	5.3 ± 0.4	-	0.13 ± 0.16	7.6 ± 6.4	-	0.21 ± 0.05

Table 1: **Data File S6, related to STAR Methods. Parameters obtained by fitting Equations 5, 8, and 9 to our calibration data.** Errors are bootstrapped as described in the STAR Methods.